WILEY VCH | small structures

RESEARCH ARTICLE OPEN ACCESS

Supraparticles from Titania Nanoplates: Assembly, Photocatalytic Polymer Encapsulation, Functionalization, and Multifunctional Hybrid Supraparticles

Jana Struck[1,2] | Lea R. Klauke[1] | Florian Schur[1] | Benedikt Sochor[3,4] | Malte Holzapfel[5] | Neus Feliu[5] | Sarathlal Koyiloth Vayalil[3,6] | Nadja C. Bigall[1,2] | Tobias Vossmeyer[1]

[1]Institute of Physical Chemistry, University of Hamburg, Hamburg, Germany | [2]The Hamburg Centre of Ultrafast Imaging, University of Hamburg, Hamburg, Germany | [3]Deutsches Elektronen-Synchrotron DESY, Hamburg, Germany | [4]Advanced Light Source, Lawrence Berkeley National Laboratory, Berkeley, California, USA | [5]Center for Applied Nanotechnology (CAN), Fraunhofer Institute for Applied Polymer Research (IAP), Hamburg, Germany | [6]Applied Science Cluster, University of Petroleum and Energy Studies (UPES), Dehradun, India

Correspondence: Tobias Vossmeyer (tobias.vossmeyer@uni-hamburg.de)

Received: 8 July 2025 | **Revised:** 17 October 2025 | **Accepted:** 27 October 2025

Keywords: assembly | encapsulation | hybrid supraparticles | iron oxide | photocatalytic polymerization | supraparticles | titania nanoparticles

ABSTRACT

This study presents the assembly of titania nanoplates (TNPs) into three-dimensional supraparticles (SPs) via an emulsion-based assembly technique using dodecyltrimethylammonium bromide (DTAB) as surfactant. The SPs have diameters ranging from ~100 to ~400 nm and are encapsulated within a polystyrene shell. The encapsulation is achieved through surface-initiated photocatalyzed radical polymerization (UVP), utilizing the intrinsic photocatalytic activity of the TNPs. By varying the duration of UV light ($\lambda = 365$ nm) exposure, the overall organic fraction of the polymer can be tuned. Small-angle X-ray scattering (SAXS) measurements indicate a higher degree of order within the SPs after the polymerization and increased interparticle distances between the encapsulated TNPs. Presumably, the polymerization initiates at the double bond of the native oleylamine ligands on the TNP surface, resulting in surface-grafting of the polymer and re-ordering of the TNPs within the encapsulated SPs. Furthermore, the functionalization of the polymer shell with carboxylic acid or azide groups is demonstrated. As a proof-of-concept, TNPs were assembled with superparamagnetic iron oxide nanocubes (SPIONs) to form hybrid SPs. The UVP could be easily adapted to these hybrid SPs, resulting in encapsulated TNP/SPION-based SPs that combine the optical and magnetic properties of both materials.

1 | Introduction

Supraparticles (SPs) are comprised of colloidal inorganic nanomaterials that agglomerate and form higher-ordered entities [1–3]. Their functionality is a combination of the individual characteristics of the nanomaterial itself and collective properties arising from the combination and synergisms of the nanomaterial building blocks, such as magnetic [4–7], catalytic [2, 8], and optical [9, 10] properties. Their synergistic functions are of great interest for applications in catalysis [2, 8, 11, 12], drug delivery [13–15], photonics [9, 10, 16, 17], sensing [18], and energy storage [19, 20]. To enable specific applications of SPs, control over their composition, size, morphology, shape, and stability is essential [1, 3, 21]. A typical synthetic route to SPs is the droplet-based template method. It commonly uses surfactant-stabilized emulsion droplets to achieve the self-assembly of nanoparticles into SPs with good control over the size of the resulting SPs [1, 2, 4, 22–24]. A common example is evaporation-induced self-assembly (EISA), which is a versatile, facile, fast, and low-cost assembly technique that allows the size of the SPs to be controlled by various parameters

[4, 24]. Emulsion-based self-assembly is a well-established approach for the preparation of SPs, which has been studied using a broad variety of nanomaterials and even the combination of different types of nanoparticles [25–27]. Other techniques, such as DNA-directed self-assembly [28, 29] or photoclick chemistry-based self-assembly [30], allow for the fabrication of more complex SP structures, but usually entail more expensive precursors or linkers and laborious modification of the nanoparticle surface [29, 30].

Besides the self-assembly of one type of nanomaterial into SPs, the co-assembly of nanomaterials with different functionality within the same hybrid SPs is of interest. One example is the combination of photocatalytic active titania and magnetic iron oxide nanoparticles. Bonnefond et al. [31] demonstrated the advancements of such multifunctional hybrid SPs for wastewater treatment. The titania photocatalyst decomposes organic compounds in the wastewater, and due to the added magnetic nanoparticles, the photocatalyst can be recovered after its usage through simple magnetic separation [31]. Similar concepts were introduced by Bagheri et al. [32] and reviewed by Pervaiz et al. [33].

Additionally, it is important to consider the stability of the assembled SPs. The synergistic properties of SPs emerge from the combination and spatial arrangement of the nanoparticle building blocks [1, 21]. It is, therefore, crucial to provide mechanically robust SPs that maintain their internal structural features during processing and application [21]. Hence, major research efforts are focusing on the development of techniques for the stabilization of SPs by their encapsulation within a polymer shell. This also enables surface-functionalization of the polymer shell, for example, for biomedical applications or the integration into other materials [34].

Currently, most encapsulation methods are based on emulsion or mini-emulsion polymerization. A very common method is the seeded emulsion polymerization. Kloust et al. [35] reported a seeded emulsion technique for iron oxide nanoparticles. The hydrophobic shells of the nanoparticles function as seeds for the following emulsion polymerization. For seed formation, the nanoparticles were injected into an aqueous polysorbate-80 surfactant solution. Next, a polystyrene shell was formed via seeded emulsion polymerization. This approach allowed the adjustment of the number of nanoparticles per seed and the polystyrene shell thickness [35]. Another example is the free radical polymerization (FRP) method developed by Schmidtke et al. [36]. However, FRP-based methods have the main drawback of uncontrolled fast termination reactions, resulting in broader molecular weight distributions and lower control over the polymer architecture [37, 38]. A solution to this problem is the controlled radical polymerization (CRP). CRP results in a much narrower molecular weight distribution and allows for improved control over the morphology [37]. Atom transfer radical polymerization (ATRP) [39–42] and reversible-addition-fragmentation chain-transfer polymerization (RAFT) [43] are the most commonly used CRP techniques. Zhu et al. [44] fabricated polymer-cadmium selenide (CdSe) quantum dot (QD) nanocomposites in a one-pot photopolymerization based on RAFT. First, they surface-modified the CdSe QDs with a RAFT agent, enabling grafting from the modified nanoparticle surface. The second step was the photoinduced electron transfer (PET) RAFT polymerization, where the CdSe QDs acted as photocatalysts. By illumination with a wavelength of 460–480 nm and the addition of a hole scavenger, they synthesized individually polymer-encapsulated QDs with tunable monomer conversion [44]. This method, as well as the example of Yan et al. [45], illustrate the photoinitiated polymer encapsulation of nanoparticles and SPs.

The photocatalytic polymerization enables a fast and energy-efficient initiation of the encapsulation of SPs at low temperatures and, in addition, enables the tunability of the polymerization rates by controlling the exposure to light and therefore, the amount of formed polymer [46, 47]. Another photocatalyst for photopolymerization is the metal oxide semiconductor titania (TiO_2). It is one of the most intensively studied photocatalysts, characterized by low cost, nontoxicity, as well as high chemical, electronic, and optical stability [48, 49]. Typical applications include water and air purification [50], gas sensing [51], as well as applications as photocatalysts, for example, for hydrogen production [52] or the initiation of polymerization [53–56]. Titania naturally exists in three main crystalline phases: rutile, anatase, and brookite [57]. The most widely used phase is anatase, with a band gap of 3.20 eV [57, 58]. It is considered to be the most active phase regarding photocatalytic activity, which likely depends on the exposed facets according to recent studies [49]. It was reported that the energetically high {001} facets have the highest photocatalytic activity. Current research is therefore focusing on the facet-controlled synthesis to obtain a high percentage of the {001} facets, for example, in titania nanoplates (TNPs) [59]. As titania only absorbs light in the UV spectral range due to its wide band gap, it is well suited for the photoinitiation or photocatalytic activation of polymerization reactions. The self-assembly of TNPs into SPs is of interest since it enables synergistic properties resulting, for example, in improved photocatalytic activity [60] or in advanced optical properties via the formation of photonic crystals [61]. In addition, the self-assembly of TNPs into ordered SPs is of interest regarding the bio-imitation of the hierarchically ordered structure of nacre, which possesses exceptional mechanical properties, such as high strength and toughness [62, 63]. In this regard, the assembly of nanoplates is beneficial, because it results in a higher theoretical packing density (∼90 vol%) [64] compared to spheres (∼75 vol%) [64, 65].

In order to obtain robust inorganic-polymer nanocomposites, surface-grafting of the polymer shell is beneficial. Several studies have been carried out in which titania was used as the photoinitiator for the polymerization based on FRP and, in some cases, CRP. Most of these photopolymerizations used vinyl monomers, acrylates, and methacrylates [53–56, 66–70]. Usually, surface-grafted photopolymerization entails surface-modification of the nanomaterial using a coupling agent [70, 71]. Typical coupling agents are double-bond-terminated silyl compounds, for example, 3-(trimethoxysilyl)propyl methacrylate (MPS) [72, 73]. A previously reported approach using individually MPS surface-modified titania nanospheres was developed by Wang et al. [72]. They implemented a photocatalytic surface-initiated polymerization on titania to fabricate well-defined core–shell nanocomposites. This approach enables tunability of the polymer shell thickness by varying the UV exposure time [72]. The main drawback of this method is the necessity of a coupling agent to enable surface-initiation. Hence, current research focuses on in situ photopolymerization without additional surface-modification of the nanomaterial. Recently, Tanaka et al. [74] reported the in situ photopolymerization on

titania nanoparticle surfaces without any pretreatment of the nanomaterial. They demonstrated the simplicity of this method using different vinyl monomers for the polymerization on either titania nanotubes or commercial titania nanoparticles [74].

In this work, we report the straightforward emulsion-based assembly of SPs from titania nanoplates (TNPs) and their facile encapsulation via a photocatalytic surface-initiated polymerization (UVP). A major advantage of this method is that no additional initiator or catalyst is required. Furthermore, no additional surface-modification of the TNPs is necessary. Presumably, the double bond of the native oleylamine ligands at the TNP surface enables surface-grafting of the polymer. The well-defined TNP-polystyrene composites were characterized using electron microscopy, Fourier-transform infrared spectroscopy (FTIR) spectroscopy, thermogravimetric analysis (TGA), and synchrotron-based small-angle X-ray scattering (SAXS). We show that the encapsulation process further increases the degree of order within the assembled SPs, and with prolonged UV exposure time, a pronounced swelling of the SPs was observed. Furthermore, the polystyrene shell could be decorated with carboxylic acid or azide groups using functionalized monomers for the UVP. To demonstrate the fabrication of multifunctional SPs, the TNPs were co-assembled into hybrid SPs with superparamagnetic iron oxide nanocubes (SPIONs). It was possible to easily adapt the UVP to these hybrid SPs, resulting in polystyrene encapsulated TNP/SPION SPs, which combine the photocatalytic and magnetic properties of both inorganic materials. Therefore, our study exemplifies the use of photocatalytically active TNPs as a general strategy for the synthesis of novel polymer-encapsulated and multifunctional hybrid SPs.

2 | Results and Discussion

2.1 | Fabrication of SPs via EISA

The starting material of this study consists of oleylamine (OLAM) stabilized TNPs with an edge length of 21.7 ± 4.2 nm and a thickness of 7.1 ± 1.3 nm. Transmission electron microscopy (TEM) images, TGA, X-ray diffraction (XRD) data of the TNPs, as well as of all the other TNP batches used in this work, are provided in the Supporting Information, Section S1. The assembly of the TNPs into three-dimensional SPs was done using an emulsion-based bottom-up approach. Here, we used the EISA approach [24]. EISA is a versatile, facile, and fast assembly technique, which allows the control over the SPs average size by varying experimental parameters such as the surfactant and nanoparticle concentration or the type of surfactant [1, 2, 4, 24, 25]. In the EISA procedure, a stable TNP dispersion in chloroform (1 mL, 12.5 mg mL^{-1}) was injected into an aqueous dodecyltrimethylammonium bromide surfactant solution (DTAB; 1 mL, 20 mg mL^{-1}) under vigorous vortexing, resulting in the formation of an emulsion. The subsequent evaporation of the organic solvent at room temperature induced the self-assembly of the TNPs into SPs. This process is schematically shown in Figure 1a. By varying the concentration of the DTAB solution (10–100 mg mL^{-1}), the size of the SPs can be controlled. Using dynamic light scattering (DLS), the z-average of the assembled SPs was determined, revealing a decreasing size of the SPs with increasing DTAB concentration (Figure 1b). This trend is in accordance with previously reported observations [4, 7]. In the following, we focused on SPs assembled using a DTAB concentration of 20 mg mL^{-1}, resulting in stable SPs with sizes ranging from ~100 to ~400 nm (determined by TEM) and a low polydispersity index (PDI) of 0.15. Two typical size histograms of SP samples that were assembled from two different TNP batches and which are based on TEM analysis, can be found in the Supporting Information, Section S4, Figure S15. Note, using a higher DTAB concentration (>30 mg mL^{-1}) resulted in the formation of significantly smaller SPs. For comparison, the DLS intensity distributions of the SPs assembled with DTAB concentrations of 10–30 mg mL^{-1} can be found in the Supporting Information, Section S5, Figure S16. The TEM images presented in Figure 1c reveal the size and shape of the assembled SPs. Some deviations from the ideal spherical shape are observed, indicating the tendency to the formation of facetted surfaces. In a set of initial experiments, we observed that an excess of OLAM ligands in the TNP batches used for the assembly process can disturb the assembly of the TNPs into SPs. Hence, we used TNP solutions that contained OLAM ligands in a concentration corresponding to roughly one monolayer coverage of the TNP surface, or less (see the Supporting Information, Table S1 and Section S6). Depending on the intended application, a more uniform size distribution of the SPs is possibly desired. In that case, the usage of

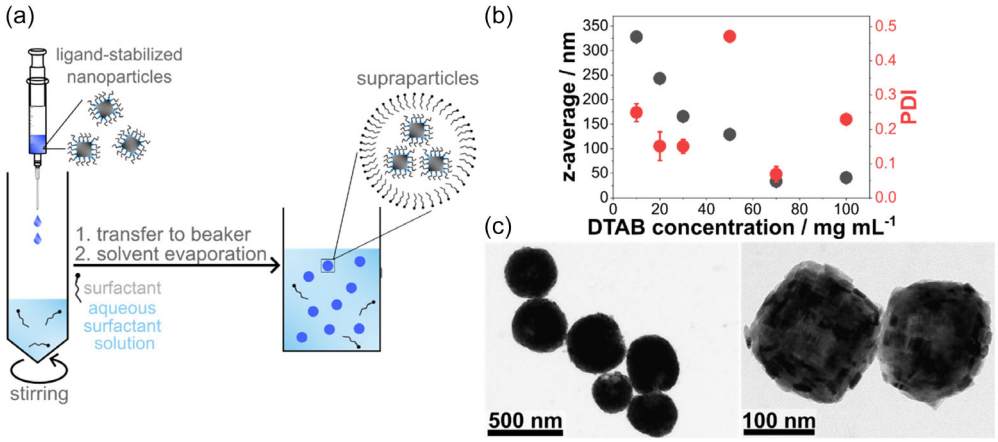

FIGURE 1 | (a) Scheme of the evaporation-induced self-assembly (EISA) of TNPs into SPs. (b) Dependency of the z-average size and the polydispersity index (PDI) of the SPs on the DTAB concentration used for the EISA process. (c) TEM images of fabricated TNP-based SPs.

microfluidic techniques can be beneficial as they enable better control over the size distribution of the SPs and the fabrication of more complex SP structures [2, 75–77].

2.2 | Photocatalytic Surface-Initiated Radical Polymerization

The method used for the encapsulation of TNP-based SPs exploits the photocatalytic activity of titania nanoparticles and was inspired by previous work of Wang et al. [72]. By exposing the TNPs to UV light, electrons are excited from the valence band into the conduction band, resulting in the formation of electron–hole pairs. If the recombination rate is low enough, the charge carriers are able to migrate to the nanoparticle's surface and undergo redox reactions [78, 79]. In this instance, and in the presence of monomers, this photoactivation enables the free radical polymerization resulting in the polymer encapsulation of the SPs. The TNPs show a strong absorption edge starting at ~380 nm with an absorbance maximum at ~254 nm, corresponding to a band gap of 3.20 eV (see the UV–vis spectra in the Supporting Information, Section S7, Figure S17). This feature is in accordance with the optical properties of TNPs reported previously [57, 58, 80].

After the assembly of the TNPs into DTAB-stabilized SPs (total TNP concentration ~8 mg mL^{-1}), as described above, the SPs were transferred into a three-necked quartz flask with additional DTAB solution (8 mL, 4.5 mg mL^{-1}) whilst stirring at 300 rpm. The suspension was saturated with nitrogen, and a 1:1 (*v*:*v*) monomer mixture (total volume 70 µL) of styrene and the crosslinker divinylbenzene [81] (DVB) was added. The suspension was continuously stirred for 5 min at 300 rpm. The monomer/SP dispersion was exposed to UV light under inert gas atmosphere using blacklight UVA lamps with a main emission peak at 365 nm (see Supporting Information, Section S24), resulting in the formation of crosslinked polystyrene (PS) shells. Figure 2 illustrates the encapsulation procedure. After the encapsulation, the SPs were separated and purified via centrifugation (see Experimental Section for details). FTIR spectroscopy of the purified SPs confirmed the formation of a polystyrene shell. The spectra shown in Figure 3b show the typical aromatic C–H stretching vibrations of polystyrene at wavenumbers ranging from 3026 to 3082 cm^{-1}. Additionally, absorption bands at wavenumbers of 1602, 1493, and 1452 cm^{-1} correspond to the aromatic C=C stretching vibrations of the benzene ring [82–84]. These specific bands are observed in the case of the

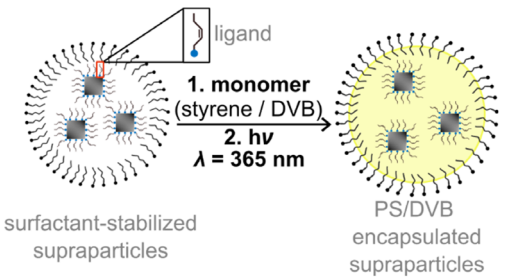

FIGURE 2 | Schematic showing the encapsulation of SPs within polystyrene (PS) shells via the UV light-induced photocatalytic free radical polymerization (UVP).

polystyrene-encapsulated SPs, but they are missing in the non-encapsulated SPs, confirming the successful formation of polystyrene. As stated above, the encapsulation procedure was inspired by the work of Wang et al. [72]. However, we conducted the polymer encapsulation on SPs assembled from TNPs without additional surface-modification, while Wang et al. encapsulated individual titania nanospheres, which were surface-modified with 3-(trimethoxysilyl)propyl methacrylate (MPS). As a major advantage, our approach to polymer-encapsulated SPs enables the synthesis of multifunctional hybrid structures consisting of different types of nanocrystals, as demonstrated below (see Section 2.5). In addition, we demonstrate the straightforward functionalization of the encapsulated SPs by simply adding different styrene derivatives to the polymerization reaction. To confirm that the UV light-induced photocatalytic free radical polymerization (UVP) is based on photocatalysis, we conducted control experiments in which we tried to initiate the polymerization thermally. These control experiments were done because the reaction mixture heated up to 42 °C due to the heat radiation of the UV reactor during the UVP reaction. In these control experiments, we did not observe any polymerization of the monomers (details can be found in the Supporting Information Section S8). To test the possible PS encapsulation via UVP without the presence of photocatalytically active titania nanoparticles, another control experiment using superparamagnetic iron oxide nanocube (SPION)-based SPs was carried out. As expected, TEM images and FTIR data (Supporting Information Section S8, Figure S18) did not indicate the formation of a PS shell, confirming that the presence of photocatalytically active nanoparticles, such as TNPs, is indeed essential for successfully conducting the UVP encapsulation of SPs. Furthermore, an additional experiment was conducted to investigate the influence of the illumination power of the UV reactor ($\lambda = 365$ nm), utilizing either 4 or 7 lamps of the reactor. The obtained data can be found in the Supporting Information, Section S9. As shown by TGA measurements, the use of 7 lamps (~31 mW cm^{-2}) resulted in the formation of only slightly more polymer than the use of 4 lamps (~16 $mWcm^{-2}$). Hence, the photoactivated polymerization reaction was almost complete after 2 h UV irradiation at both power levels. SEM images confirm that the encapsulation of the SPs was successful in both experiments.

Additionally, we tried to photocatalytically initiate the radical polymerization by exposure to deep UV (DUV) radiation using mercury UVC fluorescent lamps with a main emission peak at a wavelength of 254 nm. This wavelength matches the absorption maximum of the TNPs. However, when trying to initiate the photocatalytic polymerization using DUV radiation, we observed the spontaneous self-initiation [85] of the polymerization reaction of styrene and divinylbenzene. The PS encapsulation of the TNPs was still observable, but less selective, as the polymer was also formed without being grafted to the TNP surface. Details of this experiment can be found in the Supporting Information, Section S10. Based on this observation, it is recommended to use UV irradiation with longer wavelengths, not resulting in the self-initiated photopolymerization of the monomers. The UV reactor with a wavelength of ~365 nm, which was used in most experiments of this study, ensures the selective and well-controlled polymerization of PS at the surface of the TNPs, and hence the highly efficient encapsulation of the SPs.

By varying the UV exposure time, it was possible to tune the amount of the formed polymer, as shown by the TEM images

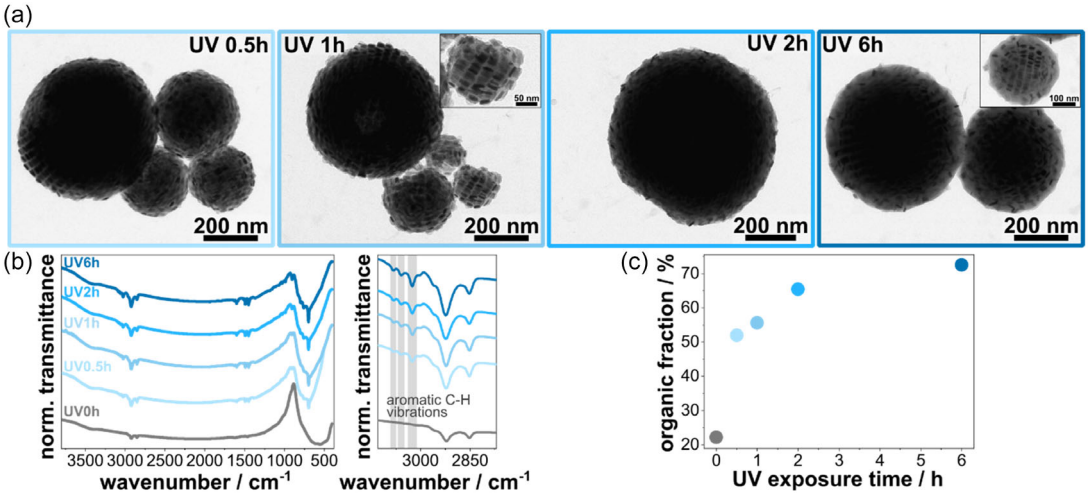

FIGURE 3 | (a) TEM images of TNP-based SPs encapsulated within polystyrene shells with increasing amount of polymer depending on the UV exposure time. (b, left) FTIR spectra of the purified nonencapsulated (gray) and encapsulated (blue) SPs with increasing UV exposure time. (b, right) Zoom into the wavenumber region from 3130 to 2770 cm^{-1} showing the aromatic C–H vibrations of PS. (c) Evolution of the organic mass fraction of the SPs with increasing UV exposure time. The organic fraction was determined via TGA (see Supporting Information, Section S11, for the TGA curves).

in Figure 3a. Furthermore, Figure 3a indicates that with progressing polymerization, the degree of ordering of the TNPs within the polymer shell near the SP surface is decreasing, especially visible after 6 h of UV exposure. The tunability of the amount of formed polymer is further confirmed by the increasing organic fraction of the SP composites (Figure 3c), which was determined using TGA of the purified samples (TGA data can be found in the Supporting Information, Section S11, Figure S21). With increasing duration of UV exposure, the organic fraction increased steeply within the first hour and then leveled off to saturation after several hours. This finding suggests that at the beginning of the reaction, the emulsion consists of surfactant-stabilized SPs and micelles containing the water-insoluble monomers. By initiating and maintaining the polymerization under UV exposure, the monomers gradually diffuse to the surface of the surfactant-stabilized SPs and are consumed in the radical polymerization reaction. When most of the monomer is consumed, the growth of the shell approaches the saturation level seen in Figure 3c. Additional experiments revealed the formation of polymeric deposits on the SP surface already after a UV exposure time of 5 min. TEM images and FTIR spectra can be found in the Supporting Information, Section S12, Figure S22.

The straightforward encapsulation as well as the well-controlled tunability of the amount of the formed polymer are advantages over other methods reported for SP encapsulation, previously, such as activators generated by electron transfer atom-transfer radical polymerization (AGET ATRP) [7, 39–42] or free radical emulsion polymerization [86–88]. A significant drawback of these methods, compared to our UVP approach, is the necessity of surface-modification in order to obtain surface-grafting of the initiator molecule to the SPs or nanoparticles. Furthermore, a catalyst or initiator needs to be added, and the time required for complete polymerization is long (~6 h) [89, 90]. The UVP encapsulation reported in this study does not require additional surface-modification with an initiator molecule, needs no additional catalyst, and is much faster.

In order to compare the UVP encapsulation of TNP-based SPs to the encapsulation via AGET ATRP, some additional experiments were conducted. To this end, we used the AGET ATRP encapsulation method developed in our previous study by Klauke et al. [7]. Details of these experiments can be found in the Experimental Section and the Supporting Information, Section S13, Figure S23. Since the AGET ATRP encapsulation requires the surface-modification of the TNPs with an initiator based on a phosphonic acid derivative, the method was much more labor-intensive than the UVP approach. In addition, the binding of the initiator molecule to the TNP surface was more difficult to achieve than in our previous study, where we used SPs from iron oxide nanocubes. Hence, the AGET ATRP encapsulation of TNP-based SPs suffered from limited reproducibility. Furthermore, the amount of formed polymer after a polymerization time of 6 h was significantly lower than in the case of the UVP method after 6 h of UV exposure (see the Supporting Information, Section S13, Figure S23b).

Moreover, our results suggest that the UVP method is also based on surface-grafting of the growing polymer shell. Wang et al. [72] modified the surface of amorphous titania nanospheres with 3-(trimethoxysilyl)propyl methacrylate (MPS), stating that these ligands provide C=C double bonds functioning as the initiation point of the polymerization and enabling the capture of photogenerated radicals. Further, they explained that the MPS ligands improve the affinity of the polymer to the titania surface, resulting in a homogenous coating of the nanoparticles [72]. In contrast, using titania nanospheres without MPS modification resulted in the formation of rough polymer coatings [72]. In our study, the TNPs were stabilized by oleylamine (OLAM) ligands. Similar as suggested by Wang et al. [72] and Ge et al. [91], it is conceivable that the double bond of the OLAM ligands is involved in the initiation of the UVP [92]. Since the IR signature of the double bond was too weak to be observed in FTIR spectra (cf. Figure 3b) our data do not evidence the reaction of the double bond. However, TEM images of single TNPs encapsulated within a PS shell as well as of encapsulated SPs, where

the PS shell is formed near and around the TNP surface reveal a surface-grafted polymerization reaction (see the Supporting Information, Section S14, Figure S24). Furthermore, the polymerization reaction resulted in rather uniform coatings on the TNPs and SPs, similar to the observations of Wang et al. [72] for titania nanospheres modified with MPS. Presumably, also other processes resulting in surface-initiation are involved. Tanaka et al. [74] reported the in situ photopolymerization on the surface of individual titania nanoparticles without any pretreatment of the nanomaterial, resulting in the formation of polymer near the nanoparticle surfaces. However, the coating appeared rougher, and the authors mentioned the presence of free polymer in the reaction solution. In our study, the PS was formed near the TNP surface and resulted in a rather homogenous coating of the SPs. Furthermore, we did not find significant amounts of free PS in the reaction solutions. In addition, the occasionally observed encapsulation of single TNPs within a PS shell suggests that the OLAM ligands located near the TNP surface enable surface-grafting of the polymer, underlining the results of Wang et al. [72].

To investigate the adaptability of the self-assembly procedure (EISA) and the UVP method to nanoparticles of different shapes, experiments with titania nanorods (TNRs) and titania nanodots (TNDs) were conducted. TEM images and FTIR spectra of the resulting SPs (see the Supporting Information, Section S15) clearly confirm the straightforward adaptability of the two procedures reported in this study.

2.3 | Internal Order and Swelling of Encapsulated SPs

The scanning electron microscopy (SEM) images shown in Figure 4a underline the tunability of the amount of formed polymer and increased swelling of the SPs with UV exposure time. Additionally, while the degree of order of the TNP assembly close to the SP surface decreases (see above, cf. Figure 3a), the degree of order in the inner volume of the SPs seems to increase with UV exposure duration. Furthermore, swelling of the SPs is indicated by increasing interparticle distances (cf. Figures 3a and 4a). The improved order is a result of the surface-grafted PS shell formed between the single TNPs (additional examples can be found in the Supporting Information, Section S16, Figure S26). This is especially visible by comparing the nonencapsulated SPs with the encapsulated SPs. Due to the surface-grafting of the polymer to the TNP surface, the PS is polymerized on the TNP surface, that is, also between the single TNPs of the assembly. Hence, the soft polymer enables the re-ordering during the encapsulation, and a higher overall degree of order within the encapsulated SPs is achieved. The increasing degree of order and the swelling effect were investigated using synchrotron-based SAXS. The scattering curves are presented in Figure 4b. The three reflections are related to the structure factor and indicate an ordered system. The comparison of the SAXS curves of the nonencapsulated (gray) and encapsulated SPs (blue) confirms the increase of order after the encapsulation, as indicated by the more pronounced reflections. The shift of the first- and second reflection to lower scattering vectors (highlighted in gray) confirms the formation of a less densely packed superlattice of TNPs within the encapsulated SPs with increasing duration of UV exposure [93]. The lattice constant d can be estimated by the relation of the scattering vector q and the Bragg condition according to Equation (1) [94]. The lattice constants were calculated using the scattering vectors of the first reflection in the SAXS curves for the different UV exposure times (see the Supporting Information Section S17).

$$d[\mathrm{nm}] = \left(\frac{2\pi}{q[\mathrm{Å}]}\right)/10 \tag{1}$$

By subtracting the average edge length of the TNPs (21.7 ± 4.2 nm) from the calculated lattice constants, one obtains an estimation of the interparticle distance between the TNPs. The values are listed in Table 1. For the nonencapsulated SPs, the interparticle distance is 2.7 nm, similar to the characteristic length of oleylamine ligands (2.05 nm) [95]. The increasing interparticle distances with increasing UV exposure time reveal progressive swelling of the TNP superlattice and, hence, the formation and growth of the PS matrix during UV exposure. Furthermore, the SEM images shown in

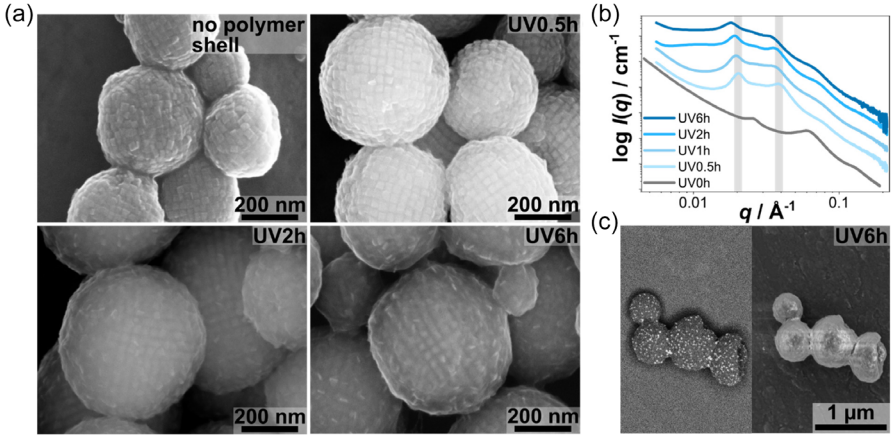

FIGURE 4 | (a) SEM images indicating an increased order of TNPs with increasing polymer content as well as pronounced swelling of the SPs. (b) SAXS curves revealing a shift of the two main reflections to lower q-values highlighted in gray with increasing UV exposure time. (c) Left: SEM image recorded with an energy-selective backscattered electron (ESB) detector revealing the migration of single TNPs within the outer growing PS shell (the contrast and brightness of the image were increased for better visibility). Right: SEM image recorded with the standard detector.

TABLE 1 | Approximate interparticle distances calculated by subtracting the average edge length of the TNPs from the calculated lattice constants obtained from the first SAXS reflection for different UV exposure times.

UV exposure time/h	Approximate interparticle distance/nm
0	2.7
0.5	9.5
1	10.1
2	10.8
6	13.1

Figure 4a confirm the concentric encapsulation of the SPs within a growing polymer shell. This is most obvious after long UV light exposure time. However, a small amount of single TNPs seems to migrate within the growing polystyrene shell, presumably due to the continuous formation of PS on the TNPs located at the SP surface. This effect is clearly visible in the SEM image recorded with an energy-selective backscattered electron (ESB) detector (Figure 4c left). Due to its higher backscatter coefficient, the TNPs embedded near the surface of the growing PS shell appear brighter than the organic PS matrix [96]. By repeating the TNP assembly into SPs and the UVP encapsulation several times, we confirmed that the protocol presented in this study provides well-reproducible results. However, occasionally we observed that the SPs formed hollow structures. Exemplary SEM images of these structures can be found in the Supporting Information, Section S18, Figure S28. The formation of such hollow structures is most likely based on the formation of a Pickering emulsion as proposed by Park et al. [97]. In Pickering emulsions [98, 99], the interface between the organic and the aqueous phase is stabilized by the surfactant and the nanoparticles. In this case, the TNPs assemble preferentially at the oil/water interface and stabilize the oil-in-water droplets. The liquid core formed inside these droplets decreases in size during solvent evaporation. Finally, when the solvent is evaporated completely, a hollow structure with a shell of assembled TNPs is formed, as occasionally observed in some SEM images.

Another important property is the long-term colloidal stability of the encapsulated SPs. Hence, DLS experiments of re-suspended SPs (ultrasonication for 2 min) were repeated 9 and 11 months after their PS encapsulation. Confirming good long-term stability in aqueous solution, the DLS size distribution profiles of these samples did not reveal any significant changes. The corresponding DLS data can be found in the Supporting Information, Section S19, Figure S29a. In addition, for biochemical applications, the colloidal stability in buffered aqueous media is of relevance. We observed a pronounced tendency of aggregation after transferring the encapsulated SPs into phosphate-buffered saline solution (PBS, pH ~7.4). In contrast, the encapsulated SPs were stable after transferring them into 50 mM HEPES (4-(2-hydroxyethyl)-1-piperazineethanesulfonic acid) buffer (pH: ~7.0). The corresponding DLS data can be found in the Supporting Information, Section S19, Figure S29b.

2.4 | Surface-Functionalization of SPs

To enable specific applications of SPs, it is often necessary to couple them to other functional molecules [34, 100]. Hence, it is desirable to decorate their surface with functional groups enabling chemical coupling reactions. As a proof-of-concept, we decorated the surface of SPs with either carboxylic acid or azide groups. This was achieved by simply substituting 10 vol% of the styrene monomers used for the UVP reaction for 4-vinylbenzoic acid or 4-vinylbenzyl azide. For these encapsulation reactions, the 1:1 (*v*:*v*) monomer mixture of styrene and the crosslinker divinylbenzene was increased to a total volume of 140 µL to obtain a thicker PS shell within a UV exposure time of 2 h. Note, varying the total volume of the monomer, whilst maintaining the UV exposure time, also enables control over the amount of the formed polymer (see the Supporting Information, Section S20). The UVP reaction with the functionalized monomers resulted in the formation of PS shells that were clearly observable in TEM images, as presented in Figure 5a. The FTIR spectra shown in Figure 5b confirm the incorporation of azide (blue) and carboxylic acid (red) groups in the PS shell. The characteristic N=N vibration of the azide group is located at a wavenumber of 2094 cm^{-1}, in accordance with the literature [101]. The incorporation of the carboxylic acid group was confirmed by the characteristic C=O vibration at a wavenumber of ~1694 cm^{-1} [102]. Additionally, the aromatic C–H stretching vibrations of PS at wavenumbers from 3026 to 3082 cm^{-1} confirm the formation of the PS shell (dark gray, red, and blue), as discussed above (cf. Figure 3b). Since a mixture of styrene and its functionalized derivatives was used for the UVP reaction, we assume that the functional groups are not exclusively located at the outer surface of the polymer shell. Most likely, the functional groups are randomly distributed within the formed polymer, that is, within the shell encapsulating the SPs and the polymer matrix formed between the TNPs.

2.5 | Multifunctional SPs Assembled from Nanocrystal Mixtures

Hybrid SPs containing different types of nanomaterials, such as semiconductors, magnetic, and plasmonic nanoparticles, have been studied by different research groups [27, 98, 103, 104]. Such combined nanomaterials enable synergistic properties which can be tailored, for example, for applications in photocatalysis [27], energy storage [103, 105], or biomedicine [105]. Here, we combined the TNPs with superparamagnetic iron oxide nanocubes (SPIONs) and assembled them using our EISA protocol into TNP/SPION hybrid SPs. This combination of nanomaterials results in a hybrid material with superparamagnetic and photocatalytic properties. Previously, Xue et al. [103] reported the assembly of iron oxide nanoparticles into a titania nanorod matrix, enabling promising application as an anode material for lithium ion storage. Other research groups combined iron oxide nanoparticles with photocatalytically active titania-based polymer composites to enable the extraction and reuse of the composite via magnetic separation [31]. Here, we used a mixture of cubic SPIONs with an edge length of ~10 nm and TNPs with an edge length of ~24 nm and a thickness of ~8 nm, with a weight fraction of 50% for each material. The TEM images of both nanomaterials are shown in Figure 6a,b (for details, see the Supporting Information, Section S1 and S21).

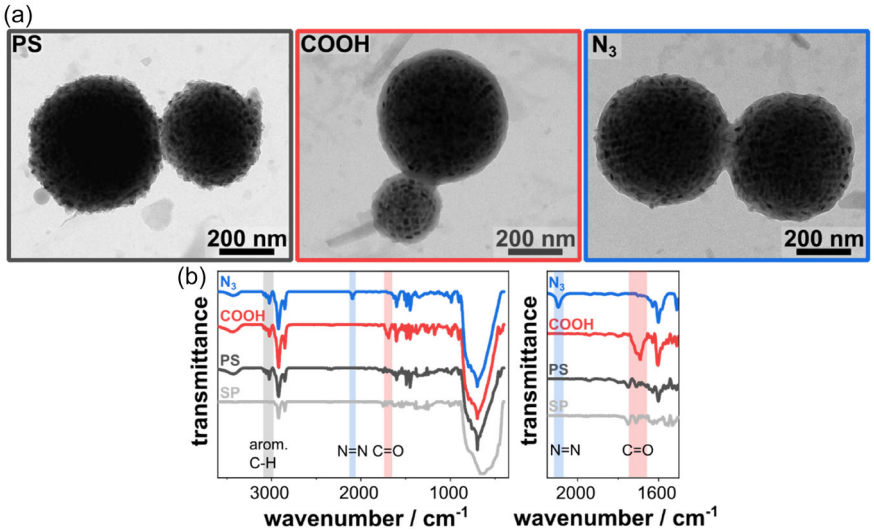

FIGURE 5 | (a) TEM images of SPs encapsulated within a nonfunctionalized (dark gray) or functionalized (red: –COOH; blue: $–N_3$) PS shell. (b, left) FTIR spectra of the nonencapsulated SPs (light gray), the SPs encapsulated with a nonfunctionalized PS shell (dark gray), and with the functionalized PS shell (red: –COOH; blue: $–N_3$). (b, right) Zoom into the wavenumber region from 2150 to 1500 cm^{-1}, showing the characteristic vibrations of the azide (highlighted in light blue) and carboxylic acid (highlighted in light red) groups.

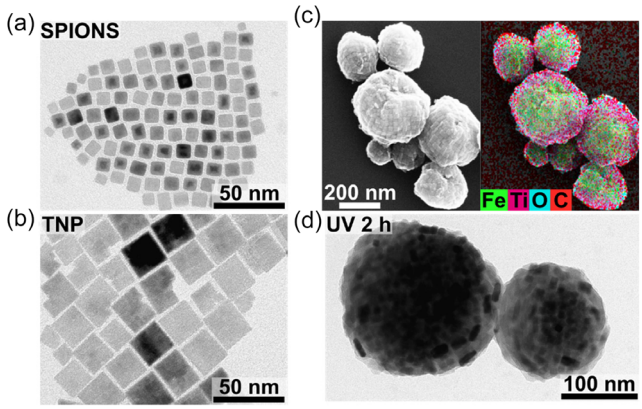

FIGURE 6 | (a,b) TEM image of the superparamagnetic iron oxide nanocubes (SPIONs) and titania nanoplates (TNPs), respectively. (c, left) SEM image of the assembled TNP/SPION hybrid SPs. (c, right) Superimposition of the EDX measurements of the TNP/SPION hybrid SPs representing the elemental distribution of iron (green), titanium (pink), oxygen (blue), and carbon (red). (d) TEM image of the PS encapsulated TNP/SPION hybrid SPs. The UVP reaction was done with a UV exposure time of 2 h.

The assembly of both materials into spherical SPs via our standard EISA protocol was straightforward. An SEM image of formed SPs is presented in Figure 6c, left. Interestingly, we observed the preferred assembly of the TNPs at the SP surface, whereas the SPIONs were mostly located in the center of the hybrid SPs. This is clearly recognized in the superimposition of the energy-dispersive X-ray spectroscopy (EDX) maps (Figure 6c, right), revealing the elements iron (green), titanium (pink), oxygen (blue), and carbon (red). As mentioned above, we also observed the tendency to form hollow hybrid SPs, presumably caused by the Pickering effect [97]. Accordingly, we attribute the preferred assembly of the TNPs at the oil/water interface to their larger size, enabling a more efficient stabilization of the oil-in-water droplets, compared to the smaller SPIONs. Taking these hybrid SPs, we demonstrated the straightforward adaptability of the developed photocatalytic surface-initiated polymerization. To this end, the UVP was conducted with a 1:1 (*v*:*v*) mixture of styrene/DVB with a UV exposure time of 2 h (for details see the Experimental Section). The TEM image of the encapsulated hybrid SPs in Figure 6d clearly confirms the formation of the PS shell. Additionally, the weight fraction of TNPs co-assembled with the SPIONs was varied to investigate its influence on the UVP encapsulation. To this end, we conducted the UVP encapsulation of TNP/SPION hybrid SPs with the following TNP/SPION ratios: 50/50, 25/75, and 10/90. The corresponding TEM images and FTIR spectra can be found in the Supporting Information, Section S22. Interestingly, the encapsulation via UVP was still feasible with only 10 wt% of titania. However, the FTIR spectra indicate that the amount of formed PS decreased significantly with the decreasing fraction of TNPs. This observation suggests that very small fractions of TNPs are sufficient to encapsulate multifunctional SPs within a polymer shell using the UVP method.

Additionally, the superparamagnetic properties of the assembled SPs were confirmed using a vibrating sample magnetometer (VSM). Data from this measurement can be found in the Supporting Information, Section S23, Figure S33a. We also added a photograph demonstrating the magnetic properties of the encapsulated hybrid SPs (Section S23, Figure S33b). In conclusion, the EISA protocol presented above should be easily adaptable to a broad variety of nanocrystal combinations. The TNPs preferentially assemble at the surface and provide the SPs with photocatalytic activity, for example, to encapsulate the SPs with a polymer shell, as demonstrated in this study.

3 | Summary and Conclusions

In this study, we reported a surface-initiated polymerization procedure for the encapsulation of TNP-based SPs which utilizes the

intrinsic photocatalytic activity of the TNPs. By illuminating the TNPs with UV light ($\lambda = 365$ nm), the polymerization is activated, resulting in the encapsulation of the SPs within a polystyrene shell. The organic fraction of the formed polymer was tuned by varying the UV exposure time. The TNPs used in this study were stabilized by OLAM ligands. According to previous works [72, 91], we assume that the double bond of the OLAM ligand is the initiation point of the UVP, thereby resulting in surface-grafting of the formed polystyrene shell. Compared to other polymerization approaches, surface-grafting without additional surface-modification and polymer encapsulation of nanomaterials without the need for an additional catalyst or initiator are a great advantage. Before the polymer encapsulation, the spherical SPs were prepared via the EISA process using DTAB as the surfactant. The EISA protocol allows for the fabrication of surfactant-stabilized SPs with sizes of approximately 100–400 nm. After assembly, the monomers (styrene/DVB) were added to the SP dispersion, and the UVP was initiated by UV illumination, resulting in the formation of the cross-linked polystyrene shell.

TEM and TGA clearly evidenced control over the amount of formed polymer by variation of the UV exposure time. The organic fraction increased with UV exposure and reached a saturation level after UV illumination for approximately 6 h. Due to the surface-initiation of the polymerization at the TNP surface, the PS is polymerized near the TNP surface, that is, on the surface of the assembled SPs as well as in-between the TNPs. Due to the formation of the soft polymer phase between the TNPs, they reorder, and a higher degree of internal order is achieved within the encapsulated SPs. Synchrotron-based SAXS measurements confirmed the increased degree of order after the encapsulation of the SPs and increasing inter-TNP distances within the SPs with increasing UVP reaction time. Furthermore, the functionalization of the polystyrene shell with carboxylic acid or azide groups was demonstrated by simply adding functionalized styrene derivatives to the monomer mixture used for the UVP reaction. To demonstrate the assembly of multifunctional SPs comprised of different types of nanomaterials, a mixture of TNPs and SPIONs was assembled into hybrid SPs. The larger TNPs preferentially assembled near the surface, while the smaller SPIONs assembled in the interior of the SPs. The combination of these materials resulted in hybrid SPs combining the photocatalytic activity of the TNPs and the superparamagnetic properties of the SPIONs. Utilizing the photocatalytic properties of the TNPs, the SPs could be encapsulated via the UVP reaction, as in the case of the SPs consisting only of TNPs.

In conclusion, the methods presented in this study provide a straightforward approach to the assembly and photocatalytically initiated polymer encapsulation of multifunctional SPs without the need for elaborate surface-modifications or additional catalysts.

4 | Experimental Section

4.1 | Materials

All chemicals were used without further purification unless otherwise stated. The solvents chloroform and tetrahydrofuran obtained from VWR were of analytical grade. Hexadecane (99%) was obtained from FLUKA. *L*-Ascorbic acid (99%), 11-(2-bromoiso-butyrate)-undecyl-1-phosphonic acid (BiB-UDPA, 95%), copper(II) bromide (99%), dodecyltrimethylammonium bromide (>98%), 4-(2-hydroxyethyl)-1-piperazineethanesulfonic acid (HEPES, >99.5%), iron oxide hydroxide (30%–60%), 1-octadecene (technical grade, 90%), oleic acid (technical grade, 90%), oleylamine (>98% primary amine), sodium oleate (>82%), and titanium(IV) chloride (100%) were obtained from Sigma–Aldrich. Titanium(IV) fluoride (>98%) was obtained from Sigma–Aldrich or Fisher scientific. Diethylene glycol (>99%), potassium bromide (Uvasol), styrene (99%), and divinylbenzene (99%, isomeric mixture) were obtained from Merck. Styrene and divinylbenzene were distilled to remove the stabilizer 4-*tert*-butylcatechol and stored at −20°C until use. Ultrapure water (resistivity 18.2 MΩcm) was obtained using an ELGA LabWater purification system (Veolia Water Solutions & Technologies, Paris, France).

4.2 | Synthesis of the Titania Nanoplates

The titania nanoplates (TNPs) were synthesized according to the procedure described by Gordon et al. [57] with minor modifications (for details see the Supporting Information, Section S1). For purification, the suspension was centrifuged at 4000 g at 15°C for 15 min. The residue was dispersed in chloroform, precipitated 1:1 (*v*:*v*) with a mixture of isopropyl alcohol and acetone with a ratio of 2:1 (*v*:*v*), and centrifuged again as described above. This step was repeated once. The resulting blue solid was dispersed in 8 mL of chloroform, and a slightly turbid blue solution was obtained. The solution was filtered with a syringe-filter (PTFE, 0.45 µm), and the filter was rinsed with ∼2 mL of chloroform. Finally, ∼10 mL of a clear blue TNP solution was obtained. **Warning**: During the TNP synthesis, hydrofluoric acid is formed in situ as a byproduct during the reaction of TiF_4 and OLAC.

A detailed overview of the properties of each used TNP batch and for which experiments each batch was used can be found in the Supporting Information, Section S1.

4.3 | Synthesis of the Titania Nanorods

The titania nanorods (TNRs) were synthesized according to the procedure described by Gordon et al. [57] with minor modifications (for details see the Supporting Information, Section S2). For purification, the suspension was centrifuged at 8000 g at 15°C for 15 min. The residue was dispersed in chloroform, precipitated 1:1 (*v*:*v*) with a mixture of isopropyl alcohol and acetone with a ratio of 2:1 (*v*:*v*), and centrifuged again as described above. This step was repeated once. The resulting yellow solid was dispersed in 6 mL of chloroform, and a slightly turbid yellow solution was obtained. The solution was filtered with a syringe-filter (PTFE, 0.45 µm), and the filter was rinsed with ∼1 mL of chloroform. Finally, ∼7 mL of a clear yellow TNR solution was obtained.

A detailed overview of the properties of the used TNR batch and for which experiment it was used can be found in the Supporting Information, Section S2.

4.4 | Synthesis of the Titania Nanodots

The titania nanodots (TNDs) were synthesized according to a procedure by Fraunhofer-Zentrum für Angewandte Nanotechnologie (for details see the Supporting Information, Section S3). For purification, the colorless precipitate was centrifuged at 8000 g at 15°C for 15 min, followed by washing with ~40 mL acetone and centrifugation at 5000 g at 15°C for 15 min. The resulting light brown residue was dried in vacuum for 3 h. The TNDs were transferred from an aqueous medium to an organic solvent via surface-modification with oleylamine according to the procedure by Hensel et al. [106] (for details see the Supporting Information, Section S3).

4.5 | SP Assembly via EISA

The TNPs were assembled into three-dimensional SPs via EISA inspired by Wang et al. [107] and Bai et al. [24]. Prior to the assembly process, a surfactant solution consisting of dodecyltrimethylammonium bromide (DTAB) in different concentrations (4.5–100 mg mL^{-1}) was prepared. In a standard procedure, 1 mL of TNPs (12.5 mg mL^{-1}) dispersed in chloroform was injected with a syringe into 1 mL of an aqueous DTAB solution (standard: 20 mg mL^{-1}) under vigorous stirring on a vortex mixer (2500 rpm). The mixing was continued for 30 s. Afterward, the formed emulsion was transferred into a beaker and stirred (300 rpm) for 60 min at room temperature, during which the chloroform evaporated. The assembled SPs were centrifuged at 2000–3000 g at 15°C for 5–10 min and dispersed in 1 mL of an aqueous DTAB solution (4.5 mg mL^{-1}). A turbid light-blue aqueous SP solution was obtained.

4.6 | Encapsulation of SPs within a Polystyrene Shell via the Photocatalytic Surface-Initiated Radical Polymerization

In a standard procedure, freshly assembled SPs (stabilized in an aqueous DTAB solution (4.5 mg mL^{-1})) were added to 8 mL of an aqueous DTAB solution (4.5 mg mL^{-1}) in a three-necked quartz flask and stirred for 15 min at 300 rpm and room temperature. The obtained suspension was saturated with nitrogen for 15 min. Next, a 1:1 (*v*:*v*) monomer mixture (total volume 70 µL) of styrene and the crosslinker divinylbenzene was added under nitrogen flow. The quartz flask setup was transferred into a custom-built UV reactor ($\lambda = 365$ nm, for details see the Supporting Information, Section S24) and stirred for 5 min at 300 rpm and room temperature. The UV exposure was started for different time periods under continuous stirring (300 rpm) and under a nitrogen atmosphere. The reaction was terminated by stopping the UV exposure and exposure to air. For purification, the encapsulated turbid, light-blue SPs were centrifuged at 3000–5000 g at 15°C for 10 min and dispersed in 2 mL of an aqueous DTAB solution (4.5 mg mL^{-1}).

4.7 | Surface-Modification and Surface-Grafted Encapsulation of SPs via AGET ATRP

The surface-modification and encapsulation of the TNP-based SPs were conducted according to the procedure by Klauke et al. [7]. For details regarding the surface-modification with the 11-(2-bromoiso-butyrate)-undecyl-1-phosphonic acid (BiB-UDPA) ligand, the preparation of the $CuBr_2$/BPMODA (*N*,*N*-bis(2-pyridylmethyl)octadecylamine) catalyst complex and the encapsulation procedure using AGET ATRP see the descriptions by Klauke et al. [7]. The encapsulation of the TNP-based SPs was conducted in a standard three-necked flask instead of the reactor setup described by Klauke et al. [7].

4.8 | Synthesis of *N*,*N*-bis(2-pyridylmethyl) octadecylamine (BPMODA)

BPMODA was synthesized according to the procedure by Kampferbeck et al. [90] based on the approach by Menger and Lee [108].

4.9 | Synthesis of 4-Vinylbenzyl Azide

The 4-vinylbenzyl azide monomer was synthesized according to the procedure by Albuszis et al. [109]. For details, see the description by Klauke et al. [7].

4.10 | Surface-Functionalization of the Polystyrene Shell with Functionalized Monomers

In order to functionalize the polystyrene shell of the TNP-based SPs with different functional groups, 70 µL (0.48 mmol) divinylbenzene, 54 µL (0.47 mmol) styrene, and 14 mg (0.094 mmol) 4-vinylbenzoic acid or 4-vinylbenzyl azide were added to the degassed surfactant-stabilized SP dispersion under stirring. Due to solubility properties, the 4-vinylbenzoic acid was dissolved in 100 µL tetrahydrofuran prior to the addition. Otherwise, the standard encapsulation procedure, as described above, was conducted.

4.11 | Synthesis of Superparamagnetic Iron Oxide Nanocubes

The superparamagnetic iron oxide nanocubes (SPIONs) were synthesized according to the procedure of Kampferbeck et al. [110]. The SPIONs had an edge length of 10.5 ± 1.0 nm and an organic fraction of either 14% (sample used for SEM EDX maps) or 8% (sample used for UVP). The native ligand on the surface of the SPIONs was OLAC. For details, see the Supporting Information, Section S21.

4.12 | Assembly of Multifunctional SPs from Nanoparticle Mixtures via EISA

The TNP/SPION hybrid SPs were assembled following the same EISA procedure as described above, with slight modifications. Instead of 1 mL of pure TNP/$CHCl_3$ solution, different ratios (wt%) of the TNPs and SPIONs (total nanoparticle concentration: 10 mg mL^{-1}; 10 mg mL^{-1} or 15 mg mL^{-1} for the UVP) dispersed in 1 mL (or 1.5 mL for the UVP) of chloroform were injected into the DTAB solution (20 mg mL^{-1}). Due to the magnetic properties

of the SPIONs, the stirring was conducted using a KPG stirrer instead of the standard magnetic stirring plate. The assembled hybrid SPs were centrifuged at 4000 g at room temperature for 5 min and dispersed in 1 mL of an aqueous DTAB solution (4.5 mg mL^{-1}). A turbid brown aqueous hybrid SP solution was obtained. The encapsulation of the TNP/SPION-based SPs via UVP was conducted as described above. Due to the magnetic properties of the SPIONs and the setup restrictions of the UV reactor, the mixture was not continuously stirred. The mixture was mixed by hand every 15 min.

4.13 | TGA

TGA was used to determine the organic mass fraction of the TNPs and the encapsulated SPs, as well as the mass concentration of the TNP solutions. The measurements were performed using a Netzsch TG 209 F1 Libra (Netzsch Gerätebau GmbH, Ahlden, Germany) device. After purification, the encapsulated SPs were centrifuged at 4000–5000 g at 15°C for 5–10 min and dispersed in ultrapure water. The SP samples were dried in an oven at ∼70°C overnight. Approximately 5–10 mg of the dried samples were transferred into an alumina crucible and put into the thermogravimeter for the TGA measurements. The following heating program was conducted whilst purging with nitrogen (40 mL min^{-1}). The samples were heated to 120°C at a rate of 10°C min^{-1} and kept for 10 min. Then, the temperature was increased to 800°C (10°C min^{-1}) and kept for 10 min. In the last step, the test chamber was purged with air (20 mL min^{-1}) for 10 min. Afterward, the ligand coverage of the TNP surface was calculated with the obtained organic fractions. A detailed description of the calculation can be found in the Supporting Information, Section S6.

4.14 | FTIR

FTIR was performed using a FTIR spectrometer, PE Spectrum Two (Perkin Elmer, Waltham, MA, United States) or a Bruker Invenio R FTIR spectrometer (Bruker, Billerica, MA, United States). All measurements were conducted whilst purging with dried air or nitrogen. After purification, the nonencapsulated and encapsulated SPs were centrifuged at 4000–5000 g at 15°C for 5–10 min and dispersed in ultrapure water. The samples were dried in an oven overnight at ∼70°C. A potassium bromide pellet was fabricated by finely blending 2–3 mg of the sample with two spatula tips of potassium bromide and subsequent pressing at ∼10 tons. For each measurement, 16 scans with a resolution of 2 cm^{-1} (PE spectrum two spectrometer) or 128 scans with a resolution of 4 cm^{-1} (Bruker Invenio R FTIR spectrometer) were collected. The FTIR spectra were recorded at wavenumbers of 4000–400 cm^{-1} and were baseline corrected with the Perkin Elmer Spectrum IR software (version: 10.7.2) or the Opus 8.1 software of Bruker. Before the measurements, a baseline of the dried air or nitrogen atmosphere was measured, and the FTIR spectra were corrected accordingly.

4.15 | TEM

TEM was performed using a JEOL JEM-1011 (JEOL, Freising, Germany; LaB_6 cathode) with an acceleration voltage of 100 kV or a FEI Tecnai G2 Spirit Twin cryo microscope (FEI, Hillsboro, OR, United States; LaB_6 cathode) operated at an acceleration voltage of 120 kV. For sample preparation, a drop of the diluted TNP or SP solution was deposited onto a carbon-coated 400-mesh copper TEM grid.

4.16 | SEM and EDX

SEM and EDX were performed using a Zeiss Leo Gemini 1550 (Zeiss, Oberkochen, Germany) with an Everhardt-Thornley detector. The measurements were conducted with the previously prepared TEM samples (as described above).

4.17 | XRD

XRD measurements were performed from 20° to 90° using a Philips X'Pert PRO MPD (Philips, Amsterdam, Netherlands) equipped with a copper K_α source ($\lambda = 0.154$ nm). To determine the crystal structure of the synthesized TNPs ∼60 µL of the TNP stock solution was drop-casted onto a silicon wafer and dried under ambient conditions. The obtained diffractograms were referenced to the diffractogram of anatase from the ICSD database [111].

4.18 | DLS

DLS was recorded using a Malvern Zetasizer Nano ZS (Malvern Panalytical, Kassel, Germany). One drop of SPs was diluted in 2 mL ultrapure water in a polymethyl methacrylate (PMMA) disposable cuvette. The samples were measured at 20°C, and three measurements were conducted with automatic measurement duration.

4.19 | Synchrotron-Based SAXS

SAXS measurements were performed at P03 of PETRA III (DESY, Hamburg, Germany) [112]. For the SAXS measurements, the X-ray wavelength was fixed at 1.023 Å with a beam size of roughly $30 \times 30\ \mu m^2$. To collect the scattering patterns, a Pilatus 2 M detector (Dectris, Baden, Switzerland) with a pixel size of 172 µm was used. The sample to detector distance was approximately 5560 ± 2 mm. For the measurements, ∼50 µL of the aqueous SP solutions (concentration: 10–20 mg mL^{-1} dispersed in an aqueous DTAB solution (4.5 mg mL^{-1})) were filled into quartz glass capillaries. These were sealed with glue and scanned over a range of 20 mm with an increment of 0.1 mm. For the data reduction of the 2D detector images to 1D scattering curves, all images corresponding to the same sample were summed up and azimuthally integrated using the PyFAI software suite [113]. The data were then scaled to absolute intensities [114] and background subtracted using well-known numerical procedures from the literature [115].

4.20 | UV–Vis Spectroscopy

UV–Vis spectroscopy was performed using a Cary 5000 UV–Vis–NIR spectrophotometer (Agilent technologies, Santa Clara,

CA, United States) equipped with an integrating sphere DRA-2500 (Labsphere, North Sutton, NH, United States). The software Cary WinUV for UV–Vis–NIR applications was used for instrument control and data collection. For the measurements, a highly diluted TNP solution (0.005 mg mL^{-1}) was prepared. Spectra were recorded in the 200–900 nm range in quartz cuvettes (optical light path 10 mm). All data were corrected with chloroform as background.

4.21 | VSM

The VSM measurement of the TNP/SPION (50/50 wt%) hybrid SPs was performed using an EZ-9 magnetometer (MicroSense, Lowell, MA, United States). The magnetization curve was measured in a range from −2.5 to 2.5 T with a step size of 100 mT between 2.5 and 0.5 T, 10 mT steps between 0.5 and 0.1 T, and 1 mT steps between 0.1 and −0.1 T. Both the forward and reverse curves were measured using the software EasyVSM 20180925-0.1. Each data set was corrected with a calibration curve of the device and an additional water measurement. The aqueous TNP/SPION hybrid SP solution (55 µL) was transferred into a 6 mm poly(ether imide) "ultem" cup, which was attached to a quartz glass rod with a parallel sample holder. The magnetization curve was normalized to the inorganic mass of the hybrid SPs obtained with a TGA measurement.

4.22 | Statistical Analysis

All FTIR spectra were normalized to [0,1] using the OriginPro 2022 or 2025 software. The scattering vector positions of the first reflection in the SAXS data were determined via peak analysis using the OriginPro 2022 or 2025 software. All DLS size distributions represent the mean of three measurements.

The size of the TNPs obtained from TEM was presented as mean ± SD. All TEM images were analyzed with the ImageJ software. To determine the average length and the thickness of the TNPs, ∼200 particles or ∼100 particles were evaluated per batch, respectively. Other results were processed with the OriginPro 2022 or 2025 software.

Author Contributions

Jana Struck: conceptualization (lead); data curation (lead); formal analysis (lead); investigation (lead); methodology (lead); validation (lead); visualization (lead); writing – original draft (lead); writing – review & editing (equal). **Lea R. Klauke**: conceptualization (supporting); data curation (supporting); formal analysis (supporting); investigation (supporting); methodology (supporting); writing – review & editing (supporting). **Florian Schur**: formal analysis (supporting); investigation (supporting); methodology (supporting). **Benedikt Sochor**: formal analysis (supporting); investigation (supporting); methodology (supporting); validation (supporting); writing – review & editing (supporting). **Malte Holzapfel**: formal analysis (supporting); investigation (supporting); methodology (supporting). **Neus Feliu**: funding acquisition (supporting); investigation (supporting); methodology (supporting); supervision (supporting). **Sarathlal Koyiloth Vayalil**: methodology (supporting); resources (supporting); supervision (supporting); validation (supporting); writing – review & editing (supporting). **Nadja C. Bigall**: funding acquisition (supporting); resources (supporting); supervision (supporting); writing – review & editing (supporting). **Tobias Vossmeyer**: conceptualization (lead); funding acquisition (lead); project administration (lead); resources (lead); supervision (lead); validation (lead); writing – review & editing (lead).

Acknowledgments

The authors acknowledge financial support from the Open Access Publication Fund of the University of Hamburg. The research was funded by the German Research Foundation (Deutsche Forschungsgemeinschaft, DFG) project ID 192346071, SFB 986, Project A1, and by the Cluster of Excellence CUI: Advanced Imaging of Matter of the German Research Foundation – EXC2056 – project ID 390715994. Neus Feliu and Malte Holzapfel acknowledge financial support by the Fraunhofer Internal Programs under Grant Attract 178-600040. The authors thank the electron microscopy service unit at the University of Hamburg, especially Charlotte Ruhmlieb, Stefan Werner, and Robert Schön, for the TEM and SEM measurements and EDX maps. Additionally, the authors thank Nina Schober from the service unit for X-ray diffraction for the XRD measurements. The authors acknowledge DESY (Hamburg, Germany), a member of the Helmholtz Association HGF, for the provision of experimental facilities. Parts of this research were carried out at PETRA III (Beamline P03). Beamtime was allocated for proposal H-20010475. The authors thank Alexander Buck for his contribution regarding some experimental procedures. Alexander Buck contributed to this project while completing an advanced practical research placement as part of his degree program.

Open Access funding enabled and organized by Projekt DEAL.

Funding

This work was suppoted by German Research Foundation (Deutsche Forschungsgemeinschaft, DFG) (192346071, 390715994); Fraunhofer Internal Programs (178-600040).

Conflicts of Interest

The authors declare no conflicts of interest.

Data Availability Statement

The data that support the findings of this study are available from the corresponding author upon reasonable request.

References

1. S. Wintzheimer, T. Granath, M. Oppmann, et al., "Supraparticles: Functionality from Uniform Structural Motifs," *ACS Nano* 12 (2018): 5093.

2. K. Hou, J. Han, and Z. Tang, "Formation of Supraparticles and Their Application in Catalysis," *ACS Materials Letters* 2 (2020): 95.

3. A. Plunkett, C. Eldridge, G. A. Schneider, and B. Domènech, "Controlling the Large-Scale Fabrication of Supraparticles," *The Journal of Physical Chemistry B* 124 (2020): 11263.

4. C. Paquet, L. Pagé, A. Kell, and B. Simard, "Nanobeads Highly Loaded with Superparamagnetic Nanoparticles Prepared by Emulsification and Seeded-Emulsion Polymerization," *Langmuir* 26 (2010): 5388.

5. A. Wolf, J. Sauer, K. Hurle, S. Müssig, and K. Mandel, "Magnetic Supraparticles Capable of Recording High-Temperature Events," *Advanced Functional Materials* 34 (2024): 2316212.

6. N. C. Bigall, M. Rodio, S. Avugadda, et al., "Scaling up Magnetic Nanobead Synthesis with Improved Stability for Biomedical Applications," *The Journal of Physical Chemistry A* 126 (2022): 9605.

7. L. R. Klauke, M. Kampferbeck, M. Holzapfel, et al., "Supraparticles from Cubic Iron Oxide Nanoparticles: Synthesis, Polymer

Encapsulation, Functionalization, and Magnetic Properties," *Langmuir* 40 (2024): 22762.

8. Z. Liu, Y. Liu, J. Yang, et al., "Highly Efficient and Controlled Fabrication of Supraparticles by Leidenfrost Phenomenon," *Langmuir* 38 (2022): 9157.

9. F. Miller, S. Wintzheimer, T. Reuter, et al., "Luminescent Supraparticles Based on CaF_2-Nanoparticle Building Blocks as Code Objects with Unique IDs," *ACS Applied Nano Materials* 3 (2020): 734.

10. E. Sowade, T. Blaudeck, and R. R. Baumann, "Self-Assembly of Spherical Colloidal Photonic Crystals inside Inkjet-Printed Droplets," *Crystal Growth & Design* 16 (2016): 1017.

11. S. Li, J. Liu, N. S. Ramesar, et al., "Single- and Multi-Component Chiral Supraparticles as Modular Enantioselective Catalysts," *Nature Communications* 10 (2019): 4826.

12. X. Zhang, M. Lin, X. Lin, et al., "Polypyrole-Enveloped Pd and Fe_3O_4 Nanoparticle Binary Hollow and Bowl-Like Superstructures as Recyclable Catalysts for Industrial Wastewater Treatment," *ACS Applied Materials & Interfaces* 6 (2014): 450.

13. Y. Yu, X. Yang, M. Liu, M. Nishikawa, T. Tei, E. Miyako, "Amphipathic Nanodiamond Supraparticles for Anticancer Drug Loading and Delivery," *ACS Applied Materials & Interfaces* 11 (2019): 18978.

14. W. Wang, C. Hao, M. Sun, L. Xu, C. Xu, and H. Kuang, "Spiky Fe_3O_4@Au Supraparticles for Multimodal In Vivo Imaging," *Advanced Functional Materials* 28 (2018): 1800310.

15. Y. Ma, C. Cortez-Jugo, J. Li, et al., "Engineering Biocoatings to Prolong Drug Release from Supraparticles," *Biomacromolecules* 20 (2019): 3425.

16. J.-G. Park, S.-H. Kim, S. Magkiriadou, T. M. Choi, Y.-S. Kim, and V. N. Manoharan, "Full-Spectrum Photonic Pigments with Non-Iridescent Structural Colors through Colloidal Assembly," *Angewandte Chemie International Edition in English* 53 (2014): 2899.

17. M. B. Bigdeli and P. A. Tsai, "Making Photonic Crystals via Evaporation of Nanoparticle-Laden Droplets on Superhydrophobic Microstructures," *Langmuir* 36 (2020): 4835.

18. S. Wintzheimer, J. Reichstein, S. Wenderoth, et al., "Expanding the Horizon of Mechanochromic Detection by Luminescent Shear Stress Sensor Supraparticles," *Advanced Functional Materials* 29 (2019): 1901193.

19. X. Zhou, Z. Li, X. Deng, et al., "High Performance Perovskite Solar Cells Using Cu_9S_5 Supraparticles Incorporated Hole Transport Layers," *Nanotechnology* 30 (2019): 445401.

20. G. Guo, L. Ji, X. Shen, et al., "Self-Assembly of Transition-Metal-Oxide Nanoparticle Supraparticles with Designed Architectures and Their Enhanced Lithium Storage Properties," *Journal of Materials Chemistry A* 4 (2016): 16128.

21. J. Wang, E. Kang, U. Sultan, et al., "Influence of Surfactant-Mediated Interparticle Contacts on the Mechanical Stability of Supraparticles," *Journal of Materials Chemistry C* 125 (2021): 23445.

22. O. D. Velev, K. Furusawa, and K. Nagayama, "Assembly of Latex Particles by Using Emulsion Droplets as Templates. 1. Microstructured Hollow Spheres," *Langmuir* 12 (1996): 2374.

23. L. Thayyil Raju, O. Koshkina, H. Tan, et al., "Particle Size Determines the Shape of Supraparticles in Self-Lubricating Ternary Droplets," *ACS Nano* 15 (2021): 4256.

24. F. Bai, D. Wang, Z. Huo, et al., "A Versatile Bottom-up Assembly Approach to Colloidal Spheres from Nanocrystals," *Angewandte Chemie International Edition* 46 (2007): 6650.

25. C. Wu, Q. Fan, and Y. Yin, "Emulsion-Confined Self-Assembly of Colloidal Nanoparticles into 3D Superstructures," *Cell Reports Physical Science* 3 (2022): 101162.

26. D. Vanmaekelbergh, L. K. van Vugt, H. E. Bakker, et al., "Shape-Dependent Multiexciton Emission and Whispering Gallery Modes in Supraparticles of CdSe/Multishell Quantum Dots," *ACS Nano* 9 (2015): 3942.

27. R. Shi, Y. Cao, Y. Bao, et al., "Self-Assembled Au/CdSe Nanocrystal Clusters for Plasmon-Mediated Photocatalytic Hydrogen Evolution," *Advanced Materials* 29 (2017): 1700803.

28. J.-W. Kim, J.-H. Kim, and R. Deaton, "DNA-Linked Nanoparticle Building Blocks for Programmable Matter," *Angewandte Chemie International Edition in English* 50 (2011): 9185.

29. A. P. Alivisatos, K. P. Johnsson, X. Peng, et al., "Organization of 'Nanocrystal Molecules' Using DNA," *Nature* 382 (1996): 609.

30. L. Chen, X. Li, and Q. Yan, "Light-Click, *In Situ*, Self-Assembly of Superhelical Nanofibers and Their Helicity Hierarchy Control," *Macromolecules* 54 (2021): 5077.

31. A. Bonnefond, M. Ibarra, E. Gonzalez, et al., "Photocatalytic and Magnetic Titanium Dioxide/Polystyrene/Magnetite Composite Hybrid Polymer Particles," *Journal of Polymer Science Part A: Polymer Chemistry* 54 (2016): 3350.

32. S. Bagheri and N. M. Julkapli, "Magnetite Hybrid Photocatalysis: Advanced Environmental Re-Mediation," *Reviews in Inorganic Chemistry* 36 (2016): 135.

33. S. Pervaiz, M. Javed, A. Shah, A. Latif, S. Nasir, and I. Shah, "Environmental Applications of Magnetite Nanohybrid Materials," *RSC Advances* 15 (2025): 19899.

34. H. Kloust, C. Schmidtke, A. Feld, et al., "*In Situ* Functionalization and PEO Coating of Iron Oxide Nanocrystals Using Seeded Emulsion Polymerization," *Langmuir* 29 (2013): 4915.

35. H. Kloust, E. Pöselt, S. Kappen, et al., "Ultrasmall Biocompatible Nanocomposites: A New Approach Using Seeded Emulsion Polymerization for the Encapsulation of Nanocrystals," *Langmuir* 28 (2012): 7276.

36. C. Schmidtke, H. Lange, H. Tran, et al., "Radical Initiated Reactions on Biocompatible CdSe-Based Quantum Dots: Ligand Cross-Linking, Crystal Annealing, and Fluorescence Enhancement," *Journal of Physical Chemistry C* 117 (2013): 8570.

37. P. Vana, ed., Advances in Polymer Science (Springer International Publishing, 2015), Vol. 270.

38. A. Butté, G. Storti, and M. Morbidelli, "Miniemulsion Living Free Radical Polymerization by RAFT," *Macromolecules* 34 (2001): 5885.

39. K. Matyjaszewski and J. Xia, "Atom Transfer Radical Polymerization," *Chemical Reviews* 101 (2001): 2921.

40. K. Min and K. Matyjaszewski, "Atom Transfer Radical Polymerization in Microemulsion," *Macromolecules* 38 (2005): 8131.

41. K. Min and K. Matyjaszewski, "Atom Transfer Radical Polymerization in Aqueous Dispersed Media," *Open Chemistry* 7 (2009): 657.

42. J.-S. Wang and K. Matyjaszewski, "Controlled/"Living" Radical Polymerization. Atom Transfer Radical Polymerization in the Presence of Transition-Metal Complexes," *Journal of the American Chemical Society* 117 (1995): 5614.

43. J. Chiefari, Y. K. Chong, F. Ercole, et al., "Living Free-Radical Polymerization by Reversible Addition-Fragmentation Chain Transfer: The RAFT Process," *Macromolecules* 31 (1998): 5559.

44. Y. Zhu and E. Egap, "PET-RAFT Polymerization Catalyzed by Cadmium Selenide Quantum Dots (QDs): *Grafting-From*, QDs Photocatalysts to Make Polymer Nanocomposites," *Polymer Chemistry* 11 (2020): 1018.

45. J. Yan, X. Pan, M. Schmitt, Z. Wang, M. R. Bockstaller, and K. Matyjaszewski, "Enhancing Initiation Efficiency in Metal-Free Surface-Initiated Atom Transfer Radical Polymerization (SI-ATRP)," *ACS Macro Letters* 5 (2016): 661.

46. S. Dadashi-Silab, M. Atilla Tasdelen, and Y. Yagci, "Photoinitiated Atom Transfer Radical Polymerization: Current Status and Future Perspectives," *Journal of Polymer Science Part A: Polymer Chemistry* 52 (2014): 2878.

47. Y. Liu, H. Zheng, Y. Wang, et al., "Synthesis of a Cationic Polyacrylamide by a Photocatalytic Surface-Initiated Method and Evaluation of Its Flocculation and Dewatering Performance: Nano-TiO_2 as a Photo Initiator," *RSC Advances* 8 (2018): 28329.

48. M. T. Noman, M. A. Ashraf, and A. Ali, "Synthesis and Applications of Nano-TiO_2: A Review," *Environmental Science and Pollution Research* 26 (2019): 3262.

49. W.-J. Ong, L.-L. Tan, S.-P. Chai, S.-T. Yong, and A. R. Mohamed, "Facet-Dependent Photocatalytic Properties of TiO_2-Based Composites for Energy Conversion and Environmental Remediation," *ChemSusChem* 7 (2014): 690.

50. V. Seiß, S. Thiel, and M. Eichelbaum, "Preparation and Real World Applications of Titania Composite Materials for Photocatalytic Surface, Air, and Water Purification: State of the Art," *Inorganics* 10 (2022): 139.

51. X. Tian, X. Cui, T. Lai, et al., "Gas Sensors Based on TiO_2 Nanostructured Materials for the Detection of Hazardous Gases: A Review," *Nano Materials Science* 3 (2021): 390.

52. M. Rafique, S. Hajra, M. Irshad, et al., "Hydrogen Production Using TiO_2-Based Photocatalysts: A Comprehensive Review," *ACS Omega* 8 (2023): 25640.

53. Y. Zhou, W. Liao, and X. Ni, "Improving Photocatalytic Free Radical Polymerization with Hydrochloric Acid," *Catalysis Science & Technology* 9 (2019): 3887.

54. C. Damm, R. Herrmann, G. Israel, and F. W. Müller, "Acrylate Photopolymerization on Heterostructured TiO_2 Photocatalysts," *Dyes and Pigments* 74 (2007): 335.

55. A. J. Hoffman, G. Mills, H. Yee, and M. R. Hoffmann, "Q-Sized CdS: Synthesis, Characterization, and Efficiency of Photoinitiation of Polymerization of Several Vinylic Monomers," *The Journal of Physical Chemistry* 96 (1992): 5546.

56. C. Dong and X. Ni, "The Photopolymerization and Characterization of Methyl Methacrylate Initiated by Nanosized Titanium Dioxide," *Journal of Macromolecular Science, Part A: Pure and Applied Chemistry* 41 (2004): 547.

57. T. R. Gordon, M. Cargnello, T. Paik, et al., "Nonaqueous Synthesis of TiO_2 Nanocrystals Using TiF_4 to Engineer Morphology, Oxygen Vacancy Concentration, and Photocatalytic Activity," *Journal of the American Chemical Society* 134 (2012): 6751.

58. D. Reyes-Coronado, G. Rodríguez-Gattorno, M. E. Espinosa-Pesqueira, C. Cab, R. de Coss, and G. Oskam, "Phase-Pure TiO_2 Nanoparticles: Anatase, Brookite and Rutile," *Nanotechnology* 19 (2008): 145605.

59. C. P. Sajan, S. Wageh, A. A. Al-Ghamdi, J. Yu, and S. Cao, "TiO_2 Nanosheets with Exposed {001} Facets for Photocatalytic Applications," *Nano Research* 9 (2016): 3.

60. W. Liu, M. Kappl, and H.-J. Butt, "Tuning the Porosity of Supraparticles," *ACS Nano* 13 (2019): 13949.

61. S. M. Klein, V. N. Manoharan, D. J. Pine, and F. F. Lange, "Synthesis of Spherical Polymer and Titania Photonic Crystallites," *Langmuir* 21 (2005): 6669.

62. U. G. K. Wegst, H. Bai, E. Saiz, A. P. Tomsia, and R. O. Ritchie, "Bioinspired Structural Materials," *Nature Materials* 14 (2015): 23.

63. J. Sun and B. Bhushan, "Hierarchical Structure and Mechanical Properties of Nacre: A Review," *RSC Advances* 2 (2012): 7617.

64. V. Semeykina, C. Appiah, S. Rothberg, S. Heinrich, D. Giuntini, and G. A. Schneider, "Expectations vs. Reality in Nacre-Like Composites: Dominating Role of Particle Packing and Polymer Confinement in Mechanical Performance," *Advanced Composites and Hybrid Materials* 8 (2025): 65.

65. D. A. Weitz, "Packing in the Spheres," *Science* 303 (2004): 968.

66. S. Singh, H. Mahalingam, and P. K. Singh, "Polymer-Supported Titanium Dioxide Photocatalysts for Environmental Remediation: A Review," *Applied Catalysis, A: General* 462-463 (2013): 178.

67. J. Yan, B. Li, F. Zhou, and W. Liu, "Ultraviolet Light-Induced Surface-Initiated Atom-Transfer Radical Polymerization," *ACS Macro Letters* 2 (2013): 592.

68. B.-F. Cheng, L.-H. Wang, and Y.-Z. You, "Photoinduced Electron Transfer-Reversible Addition-Fragmentation Chain Transfer (PET-RAFT) Polymerization Using Titanium Dioxide," *Macromolecular Research* 24 (2016): 811.

69. N. M. Ainali, D. Kalaronis, E. Evgenidou, D. N. Bikiaris, and D. A. Lambropoulou, "Insights into Biodegradable Polymer-Supported Titanium Dioxide Photocatalysts for Environmental Remediation," *Macromolecules* 1 (2021): 201.

70. X. X. Wang, H. T. Wang, X. M. Song, G. Q. Wang, Q. G. Du, and Q. T. Chen, "Photocatalytic Polymerization Induced by a Transparent Anatase Titania Aqueous Sol and Fabrication of Polymer Composites," *Express Polymer Letters* 4 (2010): 373.

71. X. Song, Y. Zhao, H. Wang, and Q. Du, "Fabrication of Polymer Microspheres Using Titania as a Photocatalyst and Pickering Stabilizer," *Langmuir* 25 (2009): 4443.

72. X. Wang, Q. Lu, X. Wang, et al., "Photocatalytic Surface-Initiated Polymerization on TiO_2 toward Well-Defined Composite Nanostructures," *ACS Applied Materials & Interfaces* 8 (2016): 538.

73. J. Zou, Y. Zhao, M. Yang, and Y. Dan, "Preparation and Characterization of Polystyrene/Titanium Dioxide Composite Particles Containing Organic Ultraviolet-Stabilizer Groups," *Journal of Applied Polymer Science* 104 (2007): 2792.

74. T. Tanaka, S. Nishimura, K. Nishiyama, et al., "Direct In Situ Polymer Modification of Titania Nanomaterial Surfaces via UV-Irradiated Radical Polymerization," *Asian Journal of Organic Chemistry* 13 (2024): e202400270.

75. T. Brugarolas, F. Tu, and D. Lee, "Directed Assembly of Particles Using Microfluidic Droplets and Bubbles," *Soft Matter* 9 (2013): 9046.

76. J. H. Kim, T. Y. Jeon, T. M. Choi, T. S. Shim, S.-H. Kim, and S.-M. Yang, "Droplet Microfluidics for Producing Functional Microparticles," *Langmuir* 30 (2014): 1473.

77. S.-K. Lee, X. Liu, V. S. Cabeza, and K. F. Jensen, "Synthesis, Assembly and Reaction of a Nanocatalyst in Microfluidic Systems: A General Platform," *Lab on a Chip* 12 (2012): 4080.

78. J. Wang, Z. Wang, W. Wang, et al., "Synthesis, Modification and Application of Titanium Dioxide Nanoparticles: A Review," *Nanoscale* 14 (2022): 6709.

79. K. Nakata and A. Fujishima, "TiO_2 Photocatalysis: Design and Applications," *Journal of Photochemistry and Photobiology, C: Photochemistry Reviews* 13 (2012): 169.

80. Y. Lan, Y. Lu, and Z. Ren, "Mini Review on Photocatalysis of Titanium Dioxide Nanoparticles and Their Solar Applications," *Nano Energy* 2 (2013): 1031.

81. R. H. Wiley, "Crosslinked Styrene/Divinylbenzene Network Systems," *Pure and Applied Chemistry* 43 (1975): 57.

82. B. C. Smith, "The Infrared Spectra of Polymers III: Hydrocarbon Polymers," *Spectroscopy* 36 (2021): 22.

83. C. Y. Liang and S. Krimm, "Infrared Spectra of High Polymers. VI. Polystyrene," *Journal of Polymer Science* 27 (1958): 241.

84. V. Hermán, H. Takacs, F. Duclairoir, O. Renault, J. H. Tortai, and B. Viala, "Core Double-Shell Cobalt/Graphene/Polystyrene Magnetic Nanocomposites Synthesized by in Situ Sonochemical Polymerization," *RSC Advances* 5 (2015): 51371.

85. Y. Zhu and E. Egap, "Light-Mediated Polymerization Induced by Semiconducting Nanomaterials: State-of-the-Art and Future Perspectives," *ACS Polymers Au* 1 (2021): 76.

86. O. Prucker and J. Rühe, "Synthesis of Poly(styrene) Monolayers Attached to High Surface Area Silica Gels through Self-Assembled Monolayers of Azo Initiators," *Macromolecules* 31 (1998): 592.

87. W. D. Harkins, "A General Theory of the Mechanism of Emulsion Polymerization," *Journal of the American Chemical Society* 69 (1947): 1428.

88. O. Prucker and J. Rühe, "Mechanism of Radical Chain Polymerizations Initiated by Azo Compounds Covalently Bound to the Surface of Spherical Particles," *Macromolecules* 31 (1998): 602.

89. L. Bai, L. Zhang, Z. Cheng, and X. Zhu, "Activators Generated by Electron Transfer for Atom Transfer Radical Polymerization: Recent Advances in Catalyst and Polymer Chemistry," *Polymer Chemistry* 3 (2012): 2685.

90. M. Kampferbeck, T. Vossmeyer, and H. Weller, "Cross-Linked Polystyrene Shells Grown on Iron Oxide Nanoparticles via Surface-Grafted AGET-ATRP in Microemulsion," *Langmuir* 35 (2019): 8790.

91. J. Ge, Y. Hu, T. Zhang, and Y. Yin, "Superparamagnetic Composite Colloids with Anisotropic Structures," *Journal of the American Chemical Society* 129 (2007): 8974.

92. X. Ding, J. Zhao, Y. Liu, H. Zhang, and Z. Wang, "Silica Nanoparticles Encapsulated by Polystyrene via Surface Grafting and in Situ Emulsion Polymerization," *Materials Letters* 58 (2004): 3126.

93. M. Krumrey, R. Garcia-Diez, C. Gollwitzer, and S. Langner, "Größenbestimmung Von Nanopartikeln Mit Röntgenkleinwinkelstreuung," *PTB-Mitt* 124 (2014): 13.

94. A. Guinier and G. Fournet, *Small-Angle Scattering of X-rays* (Wiley-VCH Verlag GmbH & Co. KGaA, 1955).

95. J. Borges, J. A. Ribeiro, E. M. Pereira, C. A. Carreira, C. M. Pereira, and F. Silva, "Preparation and Characterization of DNA Films Using Oleylamine Modified Au Surfaces," *Journal of Colloid and Interface Science* 358 (2011): 626.

96. A. Linnemann and S. Kühl, *Grundlagen der Licht- und Elektronenmikroskopie* (Verlag Eugen Ulmer, 2018).

97. J.-E. Park, M. Seo, E. Jang, H. Kim, J. S. Kim, and S.-J. Park, "Vesicle-Like Assemblies of Ligand-Stabilized Nanoparticles with Controllable Membrane Composition and Properties," *Nanoscale* 11 (2019): 1837.

98. J. Park, D. R. Hickey, S. Jun, et al., "Surfactant-Assisted Emulsion Self-Assembly of Nanoparticles into Hollow Vesicle-Like Structures and 2D Plates," *Advanced Functional Materials* 26 (2016): 7791.

99. F. G. Svensson, G. A. Seisenbaeva, N. A. Kotov, and V. G. Kessler, "Self-Assembly of Asymmetrically Functionalized Titania Nanoparticles into Nanoshells," *Materials* 13 (2020): 4856.

100. J. Guo, W. Yang, and C. Wang, "Magnetic Colloidal Supraparticles: Design, Fabrication and Biomedical Applications," *Advanced Materials* 25 (2013): 5196.

101. P. Kumar, C. Joshi, A. K. Srivastava, P. Gupta, R. Boukherroub, and S. L. Jain, "Visible Light Assisted Photocatalytic [3+2] Azide-Alkyne "Click" Reaction for the Synthesis of 1,4-Substituted 1,2,3-Triazoles Using a Novel Bimetallic Ru-Mn Complex," *ACS Sustainable Chemistry & Engineering* 4 (2016): 69.

102. R. Sukanya, D. Aruldhas, I. Hubert Joe, and S. Balachandran, "Spectroscopic and Quantum Chemical Computation on Molecular Structure, AIM, ELF, RDG, NCI, and NLO Activity of 4-VINYL Benzoic Acid: A DFT Approach," *Journal of Molecular Structure* 1253 (2022): 132273.

103. B. Xue, T. Li, B. Wang, L. Ji, D. Yang, and A. Dong, "Self-Assembled Fe_3O_4 Nanoparticle-Doped TiO_2 Nanorod Superparticles with Highly Enhanced Lithium Storage Properties," *Sustainable Energy & Fuels* 2 (2018): 616.

104. R. Borah, K. R. Ag, A. C. Minja, and S. W. Verbruggen, "A Review on Self-Assembly of Colloidal Nanoparticles into Clusters, Patterns, and Films: Emerging Synthesis Techniques and Applications," *Small Methods* 7 (2023): 2201536.

105. M. P. Pileni, ""Nano-Egg" Superstructures of Hydrophobic Nanocrystals Dispersed in Water," *Physical Chemistry Chemical Physics* 26 (2024): 16931.

106. A. Hensel, C. J. Schröter, H. Schlicke, et al., "Elasticity of Cross-Linked Titania Nanocrystal Assemblies Probed by AFM-Bulge Tests," *Nanomaterials* 9 (2019): 1230.

107. T. Wang, X. Wang, D. LaMontagne, Z. Wang, Z. Wang, and Y. C. Cao, "Shape-Controlled Synthesis of Colloidal Superparticles from Nanocubes," *Journal of the American Chemical Society* 134 (2012): 18225.

108. F. M. Menger and J. J. Lee, "Lipid-Catalyzed Transport of Cu(II) through Liquid Membranes," *The Journal of Organic Chemistry* 58 (1993): 1909.

109. M. Albuszis, P. J. Roth, F. Exnowitz, D. L. Wong, W. Pauer, and H.-U. Moritz, "Synthesis and in-Depth Characterization of Reactive, Uniform, Crosslinked Microparticles Based on Free Radical Copolymerization of 4-Vinylbenzyl Azide," *Polymer Chemistry* 7 (2016): 1168.

110. M. Kampferbeck, L. R. Klauke, H. Weller, and T. Vossmeyer, "Little Adjustments Significantly Simplify the Gram-Scale Synthesis of High-Quality Iron Oxide Nanocubes," *Langmuir* 37 (2021): 9851.

111. M. Horn, C. F. Schwerdtfeger, and E. P. Meagher, "Refinement of the Structure of Anatase at Several Temperatures," *Zeitschrift für Kristallographie* 136 (1972): 273.

112. A. Buffet, A. Rothkirch, R. Döhrmann, et al., "P03, the Microfocus and Nanofocus X-Ray Scattering (MiNaXS) Beamline of the PETRA III Storage ring: The Microfocus Endstation," *Journal of Synchrotron Radiation* 19 (2012): 647.

113. J. Kieffer, V. Valls, N. Blanc, and C. Hennig, "New Tools for Calibrating Diffraction Setups," *Journal of Synchrotron Radiation* 27 (2020): 558.

114. F. Zhang, J. Ilavsky, G. G. Long, J. P. G. Quintana, A. J. Allen, and P. R. Jemian, "Glassy Carbon as an Absolute Intensity Calibration Standard for Small-Angle Scattering," *Metallurgical and Materials Transactions A: Physical Metallurgy and Materials Science* 41 (2010): 1151.

115. B. R. Pauw, A. J. Smith, T. Snow, N. J. Terrill, and A. F. Thünemann, "The Modular Small-Angle X-Ray Scattering Data Correction Sequence," *Journal of Applied Crystallography* 50 (2017): 1800.

Supporting Information

Additional supporting information can be found online in the Supporting Information section. **Supporting Fig. S1:** (a) Representative TEM image of TNPs from batch TNP-15. (b) Normalized XRD diffractogram with the corresponding reference reflexes for anatase and the allocated crystal planes. (c) TGA graph, depicting the degradation of the organic fraction of the dried TNP-15 sample. **Supporting Fig. S2:** (a) Representative TEM image of TNPs from batch TNP-17. (b) Normalized XRD diffractogram with the corresponding reference reflexes for anatase and the allocated crystal planes. (c) TGA graph, depicting the degradation of the organic fraction of the dried TNP-17 sample. **Supporting Fig. S3:** (a) Representative TEM image of TNPs from batch TNP-19. (b) Normalized XRD diffractogram with the corresponding reference reflexes for anatase and the allocated crystal planes. (c) TGA graph, depicting the degradation of the organic fraction of the dried TNP-19 sample. **Supporting Fig. S4:** (a) Representative TEM image of TNPs from batch TNP-22. (b) Normalized XRD diffractogram with the corresponding reference reflexes for anatase and the allocated crystal planes. (c) TGA graph, depicting the degradation of the organic fraction of the dried TNP-22 sample. **Supporting Fig. S5:** (a) Representative TEM image of TNPs from batch TNP-25. (b) Normalized XRD diffractogram with the corresponding

reference reflexes for anatase and the allocated crystal planes. (c) TGA graph, depicting the degradation of the organic fraction of the dried TNP-25 sample. **Supporting Fig. S6:** (a) Representative TEM image of TNPs from batch TNP-30. (b) Normalized XRD diffractogram with the corresponding reference reflexes for anatase and the allocated crystal planes. (c) TGA graph, depicting the degradation of the organic fraction of the dried TNP-30 sample. **Supporting Fig. S7:** (a) Representative TEM image of TNPs from batch TNP-33. (b) Normalized XRD diffractogram with the corresponding reference reflexes for anatase and the allocated crystal planes. (c) TGA graph, depicting the degradation of the organic fraction of the dried TNP-33 sample. **Supporting Fig. S8:** (a) Representative TEM image of TNPs from batch TNP-33. (b) Normalized XRD diffractogram with the corresponding reference reflexes for anatase and the allocated crystal planes. (c) TGA graph, depicting the degradation of the organic fraction of the dried TNP-39 sample. **Supporting Fig. S9:** (a) Representative TEM image of TNPs from batch TNP-44. (b) Normalized XRD diffractogram with the corresponding reference reflexes for anatase and the allocated crystal planes. (c) TGA graph, depicting the degradation of the organic fraction of the dried TNP-44 sample. **Supporting Fig. S10:** (a) Representative TEM image of TNPs from batch TNP-49. (b) Normalized XRD diffractogram with the corresponding reference reflexes for anatase and the allocated crystal planes. (c) TGA graph, depicting the degradation of the organic fraction of the dried TNP-49 sample. **Supporting Fig. S11:** (a) Representative TEM image of TNPs from batch TNP-55. (b) Normalized XRD diffractogram with the corresponding reference reflexes for anatase and the allocated crystal planes. (c) TGA graph, depicting the degradation of the organic fraction of the dried TNP-55 sample. **Supporting Fig. S12:** (a) Representative TEM image of TNPs from batch TNP-67. (b) Normalized XRD diffractogram with the corresponding reference reflexes for anatase and the allocated crystal planes. (c) TGA graph, depicting the degradation of the organic fraction of the dried TNP-67 sample. **Supporting Fig. S13:** (a) Representative TEM image of TNRs from batch TNR-4. (b) Normalized XRD diffractogram with the corresponding reference reflexes for anatase and brookite. (c) TGA graph, depicting the degradation of the organic fraction of the dried TNR-4 sample. **Supporting Fig. S14:** (a) Representative TEM image of TNDs from batch TND. (b) Normalized XRD diffractogram with the corresponding reference reflexes for anatase and the allocated crystal planes. (c) TGA graph, depicting the degradation of the organic fraction of the dried TND sample. **Supporting Fig. S15:** Size distributions of self-assembled SPs obtained from the TEM images. (a) SPs based on TNPs from batch TNP-17, and (b) SPs based on TNPs from batch TNP-15. Mean particle diameters (mean) and standard deviation (SD) are indicated. **Supporting Fig. S16:** DLS intensity distributions of the purified TNP-based SPs using different DTAB concentrations and the resulting polydispersity index. **Supporting Fig. S17:** UV-vis absorption spectra of the diluted TNP-17 solution in chloroform, showing an absorption maximum around 254 nm and the start of absorption before 365 nm for the 1:8 (undiluted concentration 12.5 mg ml^{-1}) diluted TNP solution. **Supporting Fig. S18:** (a, left) TEM image of the encapsulated TNP-based SPs after UV exposure for 6 hours, (a, middle) the TNP-based SPs after the unsuccessful attempt of thermally initiated polymerization at 65 °C, and (a, right) the non-encapsulated SPION-based SPs exposed to UV light for 2 hours. (b, left) FTIR spectra of the purified non-encapsulated TNP-based SPs (grey), the TNP-based SPs after the unsuccessful attempt of thermally initiated polymerization at 35 °C (light yellow) and 65 °C (orange), the non-encapsulated SPION-based SPs exposed to UV light for 2 hours (brown), and the encapsulated TNP-based SPs (UV irradiated for 6 hours, blue). (b, right) Zoom into the wavenumber region from 3130 to 2770 cm^{-1} showing the aromatic C-H vibrations of PS. **Supporting Fig. S19:** (a) Irradiance measured at a wavelength of 365 nm when 4 or 7 lamps were switched on in the custom-built UV reactor. The measurement was conducted in the middle of the reactor for 70 seconds. (b) TGA data of TNP-based SPs encapsulated with a UV exposure time of 2 hours, utilizing either 4 or 7 lamps of the custom-built UV reactor. The second y-axis shows the temperature program applied during the TGA measurements. In the region after 98 minutes the samples were exposed to ambient atmosphere. (c) SEM images of the encapsulated TNP-based SPs utilizing 4 (black) or 7 lamps (red) of the custom-built UV reactor. **Supporting Fig. S20:** (a) TEM image of encapsulated TNP-based SPs using a custom-built deep UV reactor with a main emission peak at 254 nm. (b) TGA data of TNP-based SPs encapsulated using a UV radiation source with a main emission peak at either 365 nm (dark blue) or at 254 nm (light blue). The second y-axis shows the temperature program applied during the TGA measurements. In the region after 98 minutes the samples were exposed to ambient atmosphere. (c, left) Normalized FTIR spectrum of the encapsulated TNP-based SPs using a UV radiation source with a main emission peak at 254 nm. (c, right) Zoom into the wavenumber region from 3130 to 2770 cm^{-1} showing the aromatic C-H vibrations of the PS. **Supporting Fig. S21:** Thermogravimetric analysis of the non-encapsulated (grey) and the encapsulated (blue) SPs with increasing UV exposure time. The second y-axis shows the temperature program applied during the TGA measurements. In the region after 98 minutes the samples were exposed to ambient atmosphere. **Supporting Fig. S22:** (a) TEM images of encapsulated TNP-based SPs after 5 minutes of UV exposure. (b, left) Normalized FTIR spectra of the purified non-encapsulated (grey) and the encapsulated SPs after 5 minutes (orange) and 1 hour of UV exposure (blue). (b, right) Zoom into the wavenumber region from 3130 to 2770 cm^{-1} showing the aromatic C-H vibrations of PS (highlighted grey). **Supporting Fig. S23:** (a) TEM images of the TNP-based SPs encapsulated using AGET ATRP (pink) or the UVP method (blue) with a UV exposure time of 6 hours. (b) Organic mass fraction from the TGA measurements of the non-encapsulated SPs (grey) and the encapsulated SPs with increasing polymerization time. The pink datapoint refers to SPs encapsulated via AGET ATRP while the blue datapoints refer to SPs encapsulated via UVP with varying UV exposure times. (c, left) Normalized FTIR spectra of the purified non-encapsulated SPs (grey) and the SPs encapsulated via AGET ATRP (pink) and UVP (blue). (c, right) Zoom into the wavenumber region from 3130 to 2770 cm^{-1} showing the aromatic C-H vibrations of PS (highlighted grey). **Supporting Fig. S24:** (a) TEM image indicating the formation of the polystyrene (PS) shell around a SP near the TNP surface. (b) TEM images of encapsulated TNP-based SPs (left) and single TNPs (right) showing the formation of the PS shell near the TNP surface and validating the surface-grafting of the PS to the TiO_2 surface. **Supporting Fig. S25:** (a) TEM images of titania nanorods (TNRs, left), self-assembled TNR-based SPs (middle), and polystyrene encapsulated TNR-based SPs (right) after applying a UV exposure time of 2 hours. The TNRs had a length (l) of 24.7 nm and a diameter (d) of 2.8 nm. (b) TEM images of titania nanodots (TNDs, left), self-assembled TND-based SPs (middle), and polystyrene encapsulated TND-based SPs (right) after applying a UV exposure time of 6 hours. (c, left) Normalized FTIR spectra of the purified non-encapsulated TNR- and TND-based SPs (black and grey) and the encapsulated TNR- and TND-based SPs (brown and turquoise) after 2 hours or 6 hours UV exposure, respectively. (c, right) Zoom into the wavenumber region from 3130 to 2770 cm^{-1} showing the aromatic C-H vibrations of the PS (highlighted grey). **Supporting Fig. S26:** TEM images showing the high degree of order in the encapsulated TNP-based SPs using different TNP batches. (a) TEM images of encapsulated TNP-19-based SPs after 1 hour of UV exposure and (b) TEM image of encapsulated TNP-17-based SPs after 30 minutes of UV exposure. **Supporting Fig. S27:** SAXS curves of the non-encapsulated (a) and encapsulated TNP-based SPs with varying UV exposure time (b) 0.5 h, (c) 1 h, (d) 2 h and (e) 6 h. The scattering vector positions were determined via peak analysis of the highlighted (light yellow) q-range. **Supporting Fig. S28:** SEM images of some hollow non-encapsulated and encapsulated SPs with varying UV exposure times. **Supporting Fig. S29:** (a) DLS size distributions of TNP-based SPs encapsulated using a UV exposure time of 2 hours (blue) or 6 hours (black). The data reveal good long-term stability of the PS encapsulated SPs after 9 or 11 months, respectively. (b) DLS size distributions of TNP-based SPs encapsulated using a UV exposure time of 2 hours. The data reveal good colloidal stability of the PS encapsulated SPs after transfer into 50 mM HEPES (4-(2-hydroxyethyl)-1-piperazineethanesulfonic acid) buffer. The data were recorded directly after the transfer into the buffer and 24 h later, as indicated. **Supporting Fig. S30:** (a) TEM images of encapsulated TNP-based SPs with increasing total monomer volume for a UV exposure time of 2 hours. (b) TGA data of the non-encapsulated (yellow) and encapsulated SPs with increasing total monomer volume for a UV exposure time of 2 hours. (c) FTIR spectra of the purified non-encapsulated SPs (yellow) and the encapsulated SPs with increasing total monomer volume for a UV exposure time of 2 hours. The highlighted area (grey) show the vibrations of the aromatic C-H groups representing the formed PS.

Supporting Fig. S31: (a) Representative TEM image of the SPIONs ($Fe10_{14}$). The subscript represents the organic fraction of the SPION sample. (b) Size histogram of the SPIONs ($Fe10_{14}$). (c) TGA graph, depicting the degradation of the organic fraction of the dried SPIONs sample $Fe10_{14}$ (grey) and with one additional precipitation step $Fe10_{8}$ (red). **Supporting Fig. S32:** (a) TEM images of the encapsulated TNP/SPION hybrid SPs with decreasing TNP/SPION ratios from left to right. The hybrid SPs were encapsulated by applying a UV exposure time of 2 hours. (b, left) Normalized FTIR spectra of the purified encapsulated TNP/SPION hybrid SPs with a TNP/SPION ratio of 50/50 (dark grey), 25/75 (red), and 10/90 (blue). (b, right) Zoom into the wavenumber region from 3130 to 2770 cm^{-1} showing the aromatic C-H vibrations of the PS (highlighted grey). **Supporting Fig. S33:** (a) Magnetization curve of TNP/SPION hybrid SPs, using a weight fraction of 50% for each material, obtained from a VSM measurement. (b, left) Photograph of the encapsulated TNP/SPION hybrid SPs suspension. (b, right) Photograph of the encapsulated TNP/SPION hybrid SPs suspension standing beside a magnet (NdFeB blockmagnet, N40), indicating the magnetic properties of the encapsulated hybrid SPs. **Supporting Fig. S34:** (a) Photograph of the entire custom-built UV reactor (left) and the interior of the UV reactor showing four of the eight UVA lamps. (b) Emission spectrum of two lamps of the custom-built UV reactor with a main emission peak at ∼365 nm. (c) Irradiance measured directly in front of the individual lamp at a wavelength of 365 nm for two lamps of the custom-built UV reactor during 60 seconds. **Supporting Table S1:** Overview of the TNP batches with edge length, thickness, crystal phase, organic fraction, and calculated amount of ligand monolayers. **Supporting Table S2:** Overview of the experiments conducted with the various TNP batches. **Supporting Table S3:** Overview of the TNR batch with edge length, thickness, crystal phase, organic fraction, and calculated amount of ligand monolayers. **Supporting Table S4:** Overview of the TND batch with diameter, crystal phase, organic fraction, and calculated amount of ligand monolayers. **Supporting Table S5:** The scattering vectors were determined via peak analysis of the first reflection in the SAXS curves for different UV exposure times. The lattice constant was calculated with the scattering vectors using equation 1 from the main document. The approximate interparticle distances were calculated by subtracting the average edge length of the TNPs (21.7±4.2 nm) from the calculated lattice constants.